

cy.3

EAVES

JAN 9 1974

MAR 13 1974



HEAT-TRANSFER TESTS ON A 14-PERCENT-SCALE MODEL OF THE NASA-MMC VIKING MARS ENTRY VEHICLE AT MACH NUMBER 16

Herbert R. Little and A. H. Boudreau
ARO, Inc.

VON KÁRMÁN GAS DYNAMICS FACILITY
ARNOLD ENGINEERING DEVELOPMENT CENTER
AIR FORCE SYSTEMS COMMAND
ARNOLD AIR FORCE STATION, TENNESSEE 37389

December 1973

Final Report for Period March 20 — April 6, 1973

Approved for public release; distribution unlimited.

Prepared for

NATIONAL AERONAUTICS AND SPACE ADMINISTRATION
LANGLEY RESEARCH CENTER
HAMPTON, VIRGINIA 23365

RECEIVED
AEDC LIBRARY
F40600-74-5000

NOTICES

When U. S. Government drawings specifications, or other data are used for any purpose other than a definitely related Government procurement operation, the Government thereby incurs no responsibility nor any obligation whatsoever, and the fact that the Government may have formulated, furnished, or in any way supplied the said drawings, specifications, or other data, is not to be regarded by implication or otherwise, or in any manner licensing the holder or any other person or corporation, or conveying any rights or permission to manufacture, use, or sell any patented invention that may in any way be related thereto.

Qualified users may obtain copies of this report from the Defense Documentation Center.

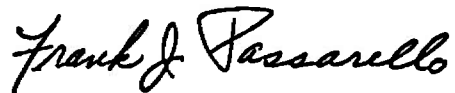
References to named commercial products in this report are not to be considered in any sense as an endorsement of the product by the United States Air Force or the Government.

APPROVAL STATEMENT

This technical report has been reviewed and is approved.



JIMMY W. MULLINS
Lt Colonel, USAF
Chief Air Force Test Director, VKF
Directorate of Test



FRANK J. PASSARELLO
Colonel, USAF
Director of Test

7360

UNCLASSIFIED

SECURITY CLASSIFICATION OF THIS PAGE (When Data Entered)

REPORT DOCUMENTATION PAGE		READ INSTRUCTIONS BEFORE COMPLETING FORM
1. REPORT NUMBER AEDC-TR-73-195	2. GOVT ACCESSION NO.	3. RECIPIENT'S CATALOG NUMBER
4. TITLE (and Subtitle) HEAT-TRANSFER TESTS ON A 14-PERCENT-SCALE MODEL OF THE NASA-MMC VIKING MARS ENTRY VEHICLE AT MACH NUMBER 16		5. TYPE OF REPORT & PERIOD COVERED Final Report - March 20 to April 6, 1973
		6. PERFORMING ORG. REPORT NUMBER
7. AUTHOR(s) Herbert R. Little and A. H. Boudreau, ARO, Inc.		8. CONTRACT OR GRANT NUMBER(s)
9. PERFORMING ORGANIZATION NAME AND ADDRESS Arnold Engineering Development Center (XO) Arnold Air Force Station, Tenn. 37389		10. PROGRAM ELEMENT, PROJECT, TASK AREA & WORK UNIT NUMBERS Program Element 921E-5 Task 9620
11. CONTROLLING OFFICE NAME AND ADDRESS National Aeronautics and Space Admin. Langley Research Center Langley, Virginia 23365		12. REPORT DATE December 1973
		13. NUMBER OF PAGES 52
14. MONITORING AGENCY NAME & ADDRESS (if different from Controlling Office)		15. SECURITY CLASS. (of this report) UNCLASSIFIED
		15a. DECLASSIFICATION/DOWNGRADING SCHEDULE N/A
16. DISTRIBUTION STATEMENT (of this Report) Approved for public release; distribution unlimited.		
17. DISTRIBUTION STATEMENT (of the abstract entered in Block 20, if different from Report)		
18. SUPPLEMENTARY NOTES Available in DDC		
19. KEY WORDS (Continue on reverse side if necessary and identify by block number) laminar boundary layer design criteria heat transfer stagnation point wind tunnel test hotshot wind tunnels environmental simulation scale model Mach number		
20. ABSTRACT (Continue on reverse side if necessary and identify by block number) Experimental laminar boundary-layer heat-transfer-rate data are presented for the NASA-MMC Viking Mars Entry Vehicle at Mach number 16 and Reynolds numbers from 0.5×10^6 to 0.9×10^6, based on a model diameter of 19.3 in. Testing was conducted at angles of attack from 0 to -16 deg. Using the stagnation heat-transfer rate for a hemisphere of the same nose radius as the Viking as a reference value, the stagnation point heat-transfer rates on the Viking front face were found to be about 60 percent of the		

UNCLASSIFIED

SECURITY CLASSIFICATION OF THIS PAGE(When Data Entered)

reference value. Near the windward edge of the front face at pitch angles of -11.2 and -16 , heating rates were 100 percent of the hemisphere value. Maximum heating rates on the base cover were about 2.5 percent of the reference hemisphere value. Local interference heating amplification factors were found to be as high as a factor of four downstream of a protruding front-face surface feature, but less than two for front-face cavities.

A-40
Amcic A 5 T.11

UNCLASSIFIED

SECURITY CLASSIFICATION OF THIS PAGE(When Data Entered)

PREFACE

The work reported herein was conducted by the Arnold Engineering Development Center (AEDC), Air Force Systems Command (AFSC), under the sponsorship of the National Aeronautics and Space Administration (NASA) Langley Research Center for the Martin-Marietta Corporation, Denver, Colorado. The work was done by ARO, Inc. (a subsidiary of Sverdrup & Parcel and Associates, Inc.), contract operator of the AEDC, Arnold Air Force Station, Tennessee. The ARO Project No. was VA286. The manuscript (ARO Control No. ARO-VKF-TR-73-132) was submitted for publication on September 24, 1973.

The authors acknowledge the assistance of Dr. John Adams, Mr. E. O. Marchand, and Dr. A. W. Mayne, Jr., (AEDC-VKF) in preparing the analytical data presented in this report.

CONTENTS

	<u>Page</u>
1.0 INTRODUCTION	5
2.0 APPARATUS	
2.1 Tunnel and Nozzle Description	5
2.2 Model	8
2.3 Instrumentation	13
3.0 PROCEDURE	
3.1 Test Conditions and Procedures	16
3.2 Data Acquisition and Reduction	18
3.3 Data Precision	19
4.0 SUMMARY OF RESULTS	22
5.0 CONCLUDING REMARKS	38
REFERENCES	39

ILLUSTRATIONS

Figure

1. AEDC-VKF Tunnel F	
a. Tunnel F Plant	6
b. Viking Model Installation in the 108-in. Test Section	7
2. Photographs of Viking Model	
a. Model and Sting	9
b. Aeroshell (Front Face)	9
c. Aeroshell Surface Features	10
d. Base Cover (Back Face)	10
3. Model Dimensions and Instrumentation	
a. Assembly.	11
b. Surface Feature and Interference Field Details	12
4. Typical Timewise Variation of Tunnel Conditions and Model Data	
a. Typical Analog Output	20
b. Digital Data Output	20
5. Summary of Base Pressure Data	23
6. Comparison of Analog Signal with Calculated Heat-Transfer Rate - Coaxial Thermocouple Transducer	25

<u>Figure</u>	<u>Page</u>
7. Summary of Aeroshell (Front Face) Pressure Data	26
8. Summary of Aeroshell (Front Face) Heat-Transfer-Rate Data	
a. $\alpha_A = 0$ deg	27
b. $\alpha_A = -6.0$ deg	28
c. $\alpha_A = -11.2$ deg	29
d. $\alpha_A = -16.0$ deg	30
9. Heat-Transfer-Rate Data	
a. UAMS Interference Field	32
b. RPA Interference Field	33
c. IFP Interference Field	34
10. Summary of Base Cover Heat-Transfer-Rate Data	
a. $\alpha_{BC} = 0$ deg	35
b. $\alpha_{BC} = \pm 6$ deg	35
c. $\alpha_{BC} = \pm 11.2$ deg	36
d. $\alpha_{BC} = \pm 16$ deg	37

TABLES

1. Gage and Surface Feature Locations	14
2. Summary of Test Conditions	17
3. Run Schedule	17
4. Number of Gages Corrected by Fairing for Particle Influences on a Given Run	26

APPENDIX

A. Evaluation of Shock Shapes and Flow Field Nonuniformities . .	41
NOMENCLATURE	49

1.0 INTRODUCTION

The Viking Mars Lander vehicle is to be protected during the Martian entry by a 70-deg half-angle, spherically blunted, conical heat shield designated as the aeroshell. The aeroshell surface contains several surface features (protuberances and cavities) associated with mechanical fittings and entry instrumentation. Heat-transfer rates in the vicinity of such features are known to be significantly affected, with local heat-transfer-rate amplification being dependent on the feature geometry and the flow environment (see, for example, Ref. 1). The test program described herein was initiated to verify the adequacy of the design criteria for the aeroshell and base cover heat shields.

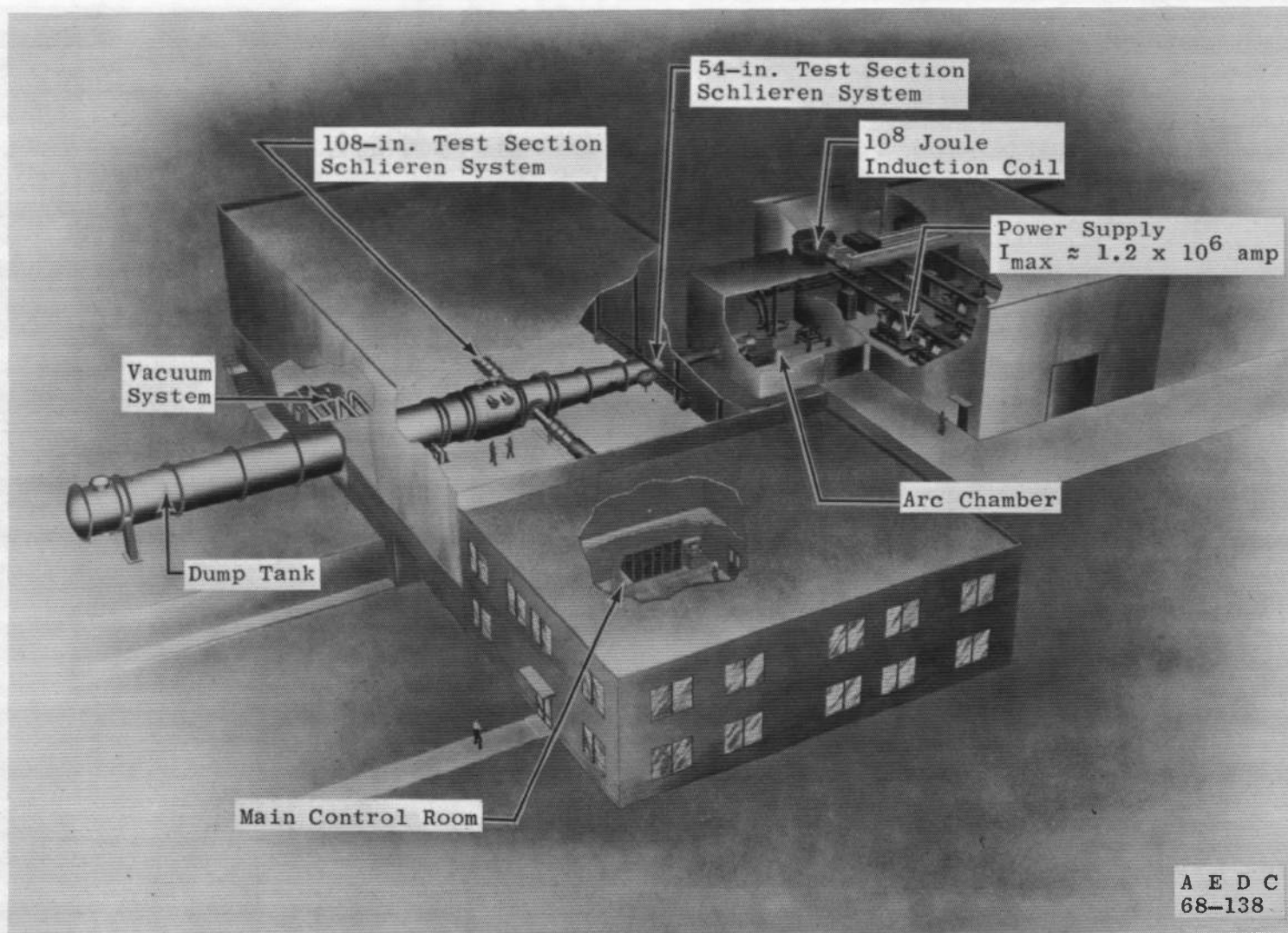
The experimental data presented were obtained in the Hypervelocity Wind Tunnel (F) of the von Kármán Facility at a free-stream Mach number of 16 and Reynolds numbers from 0.5 to 0.9×10^6 , based on model base diameter.

2.0 APPARATUS

2.1 TUNNEL AND NOZZLE DESCRIPTION

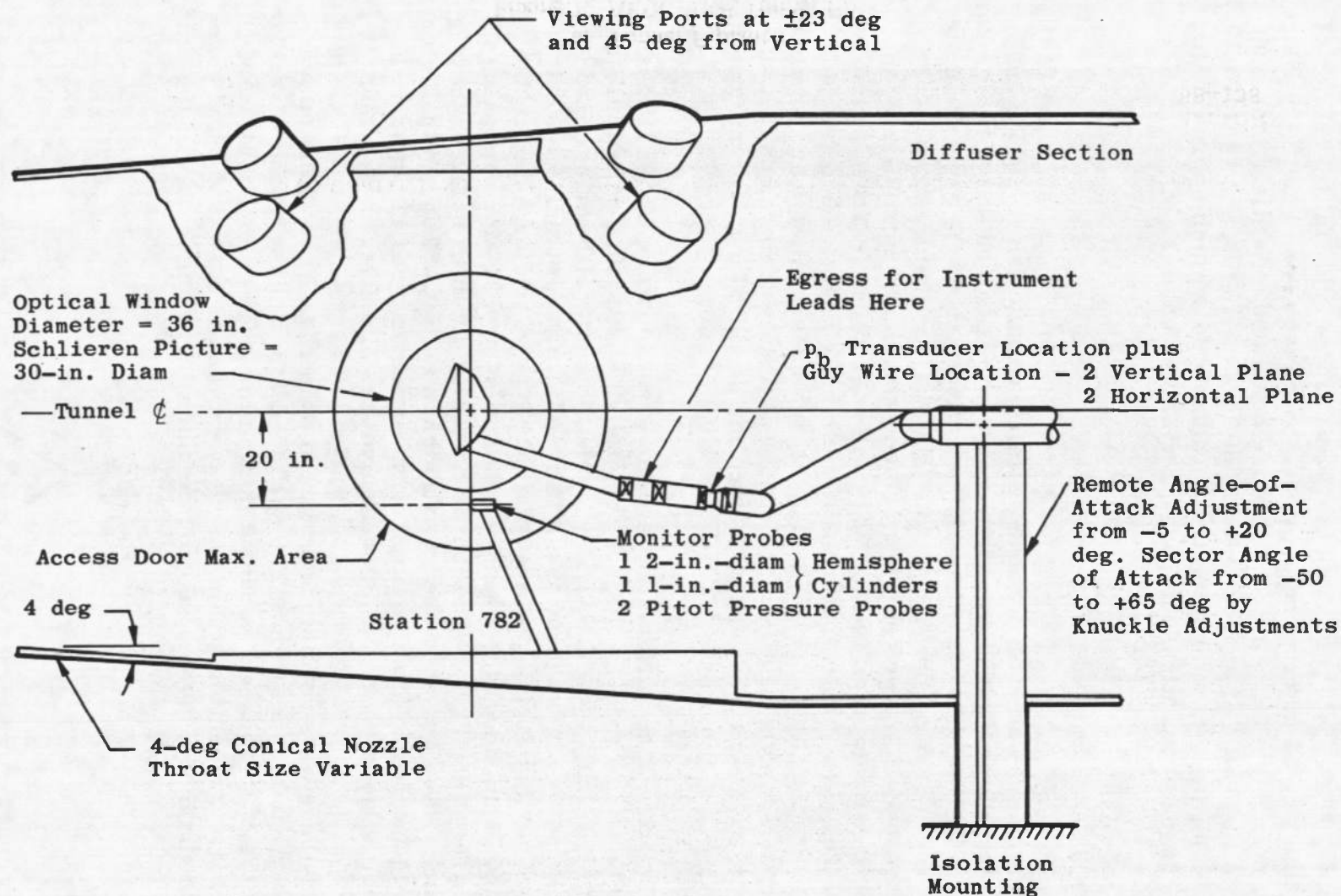
Tunnel F is an arc-driven wind tunnel of the hotshot type (Ref. 2) capable of providing Mach numbers from about 7.5 to 20 over a Reynolds-number-per-ft range from 0.05×10^6 to 75×10^6 . As shown in Fig. 1a, test sections of 108-in. diameter (free-stream Mach number, $M_\infty = 14$ to 20) and 54-in. diameter ($M_\infty = 10$ to 16) are available using a 4-deg half-angle conical nozzle. The range of Mach numbers at a particular test station in the conical nozzle is obtained by using various throat diameters. The $M_\infty = 8$ contoured nozzle has a 25-in. exit diameter which connects to the 54-in.-diam test station and provides a free-jet exhaust. The test gas, which can be either air or nitrogen, is initially confined in either a 2.5- or a 4.0-ft³ arc chamber where it is heated and compressed by an electric arc discharge. The increase in pressure results in a diaphragm rupture with the subsequent flow expansion through the nozzle. Test times are typically from 50 to 200 msec. Shadowgraphs and schlieren coverage are available at both test sections.

This test was conducted in the 108-in.-diam test section of the conical nozzle for $M_\infty = 16$, as shown in Fig. 1b, with nitrogen as the



a. Tunnel F plant

Figure 1. AEDC-VKF Tunnel F.



b. Viking model installation in the 108-in. test section
Figure 1. Concluded.

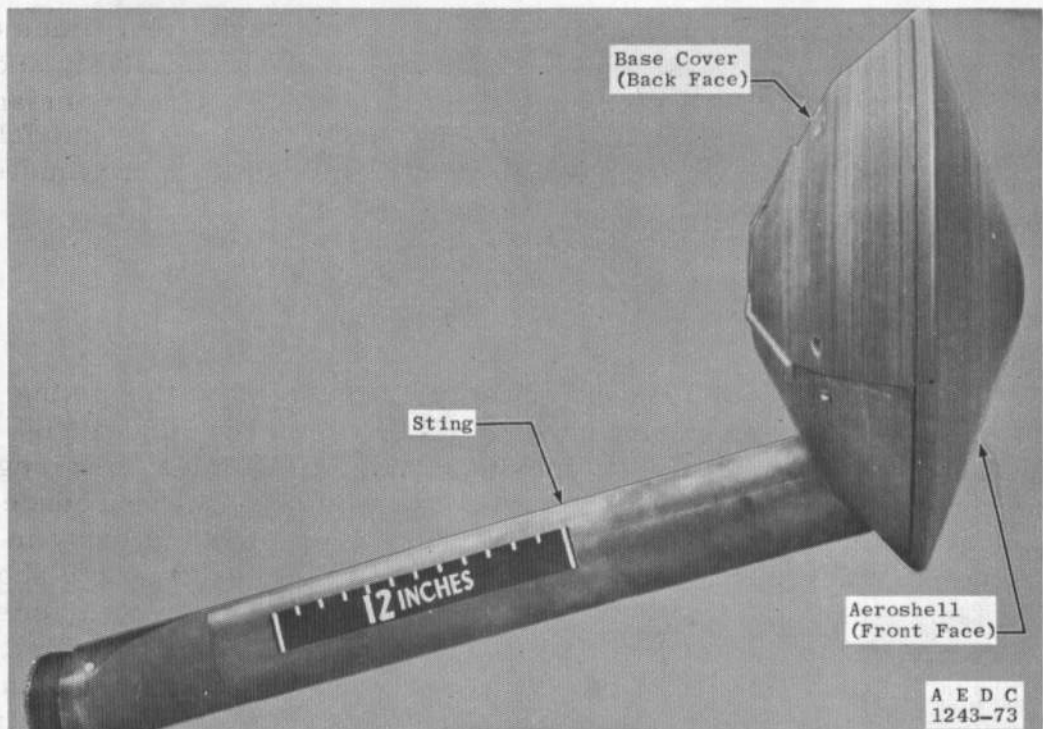
test gas. The 2.5-ft³ arc chamber was used, and useful test times of approximately 60 msec were obtained. Because of the relatively short test times, the model wall temperature remained essentially constant at the initial value of approximately 540°R, and $T_w/T_o \approx 0.14$ (model wall temperature to stagnation temperature ratio) which approximates the condition of practical interest for reentry vehicles.

2.2 MODEL

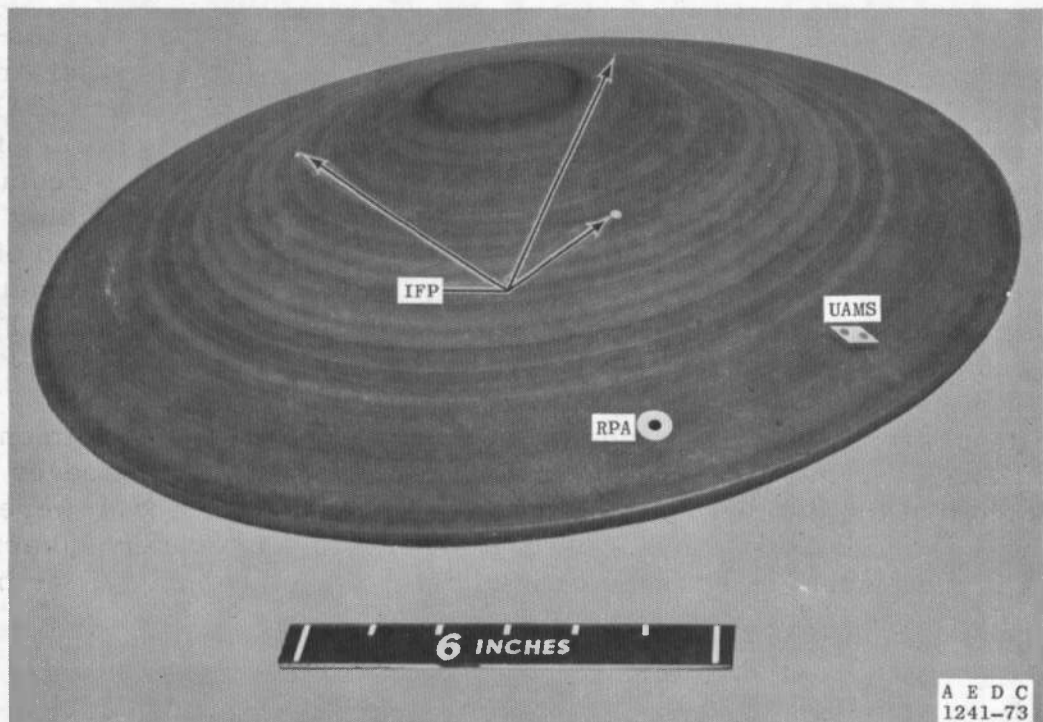
The model was a 14-percent-scale representation of the Viking Entry Vehicle and is shown mounted on its knife-edged sting in Fig. 2a. The aeroshell or front face is a spherically blunted, 70-deg half-angle cone, shown separately in Fig. 2b. The surface features reproduced on the aeroshell are noted in Fig. 2b and are shown more clearly in the detailed photograph in Fig. 2c. The base cover features are shown in Fig. 2d. Although there are features on the flight vehicle surface not included on the Tunnel F model, all features omitted were smaller than those shown. Details of the model assembly dimensions and surface feature geometries are presented in Fig. 3, along with the instrumentation locations.

The front-face surface features included were the Upper Atmosphere Mass Spectrometer Cover (UAMS), the Retarding Potential Analyzer (RPA), and the Aeroshell/Bioshield Structural Interface Pad (IFP) which occurs in three locations. The UAMS is a protruding cover of trapezoidal shape having a height of 0.123 in. The RPA is a circular cavity 0.14 in. deep with a surface diameter of 0.210 in. expanding to a diameter of 0.427 in. The IFP is basically a hemispherical cup of 0.07-in. radius centered over a cylindrical hole 0.062 in. in diameter and 0.34 in. deep. A photograph of the three features is shown in Fig. 2c, and the geometric details of the features are given in Fig. 3b.

The base cover of the model is shown in Fig. 2d, and the dimensions are given in Fig. 3a. The surface feature shown is the cover for the bridle of the descent parachute. The threaded holes shown were for access to mounting screws used to secure the base cover and aeroshell to the model central support member. Upon assembly of the model, the holes were filled with faired plugs.

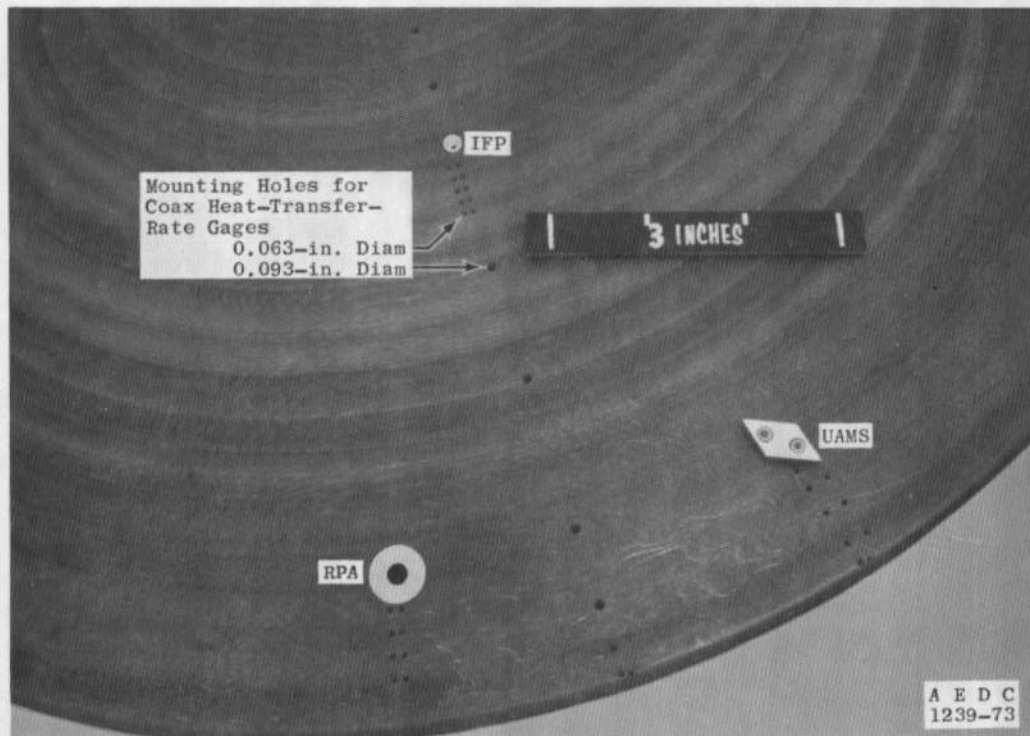


a. Model and sting

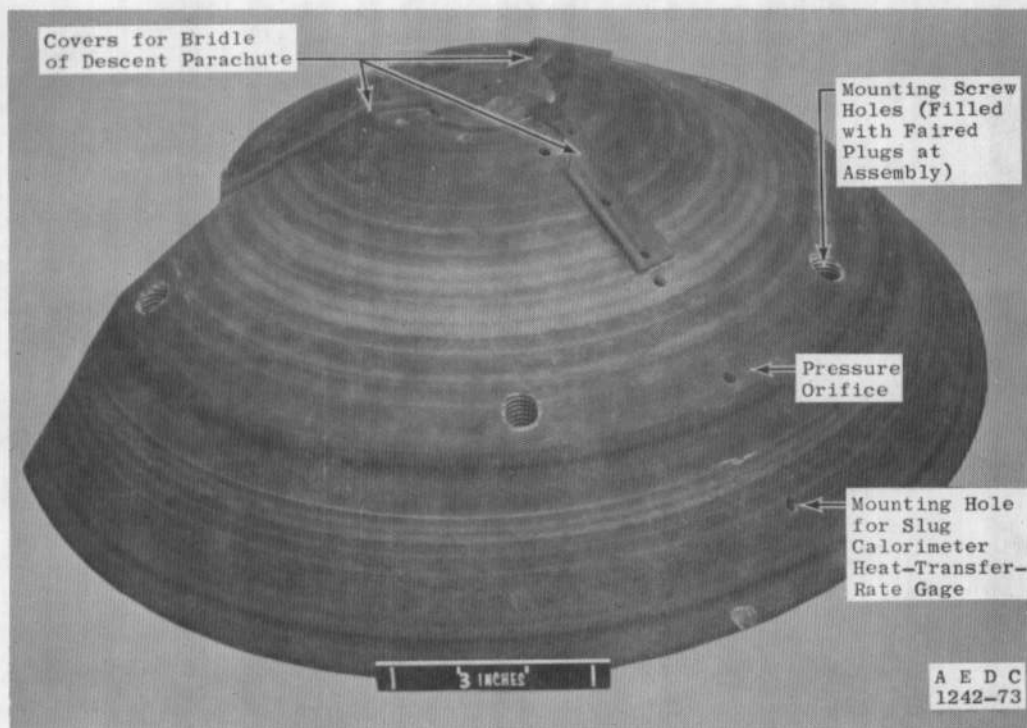


b. Aeroshell (front face)

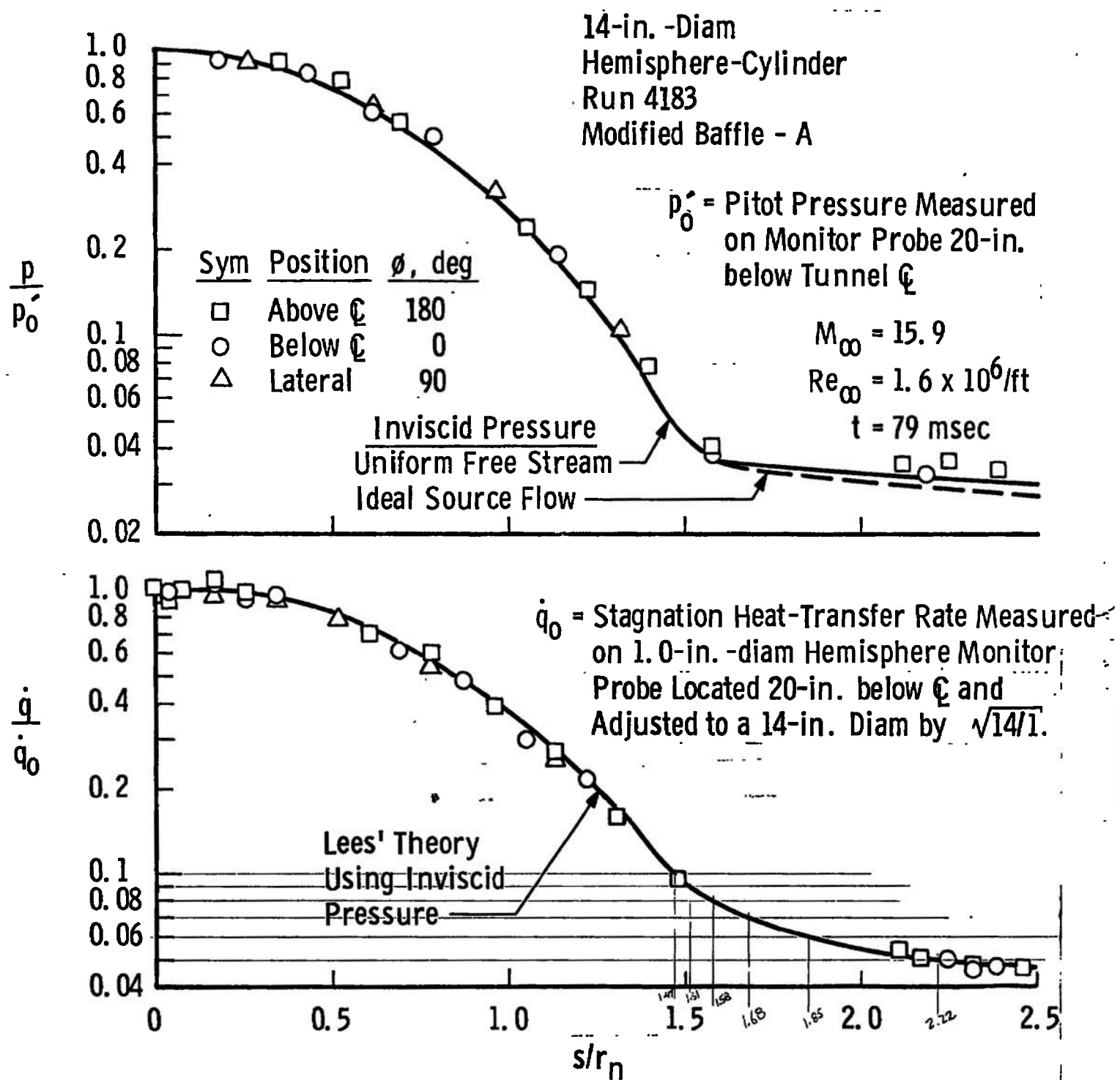
Figure 2. Photographs of Viking model.



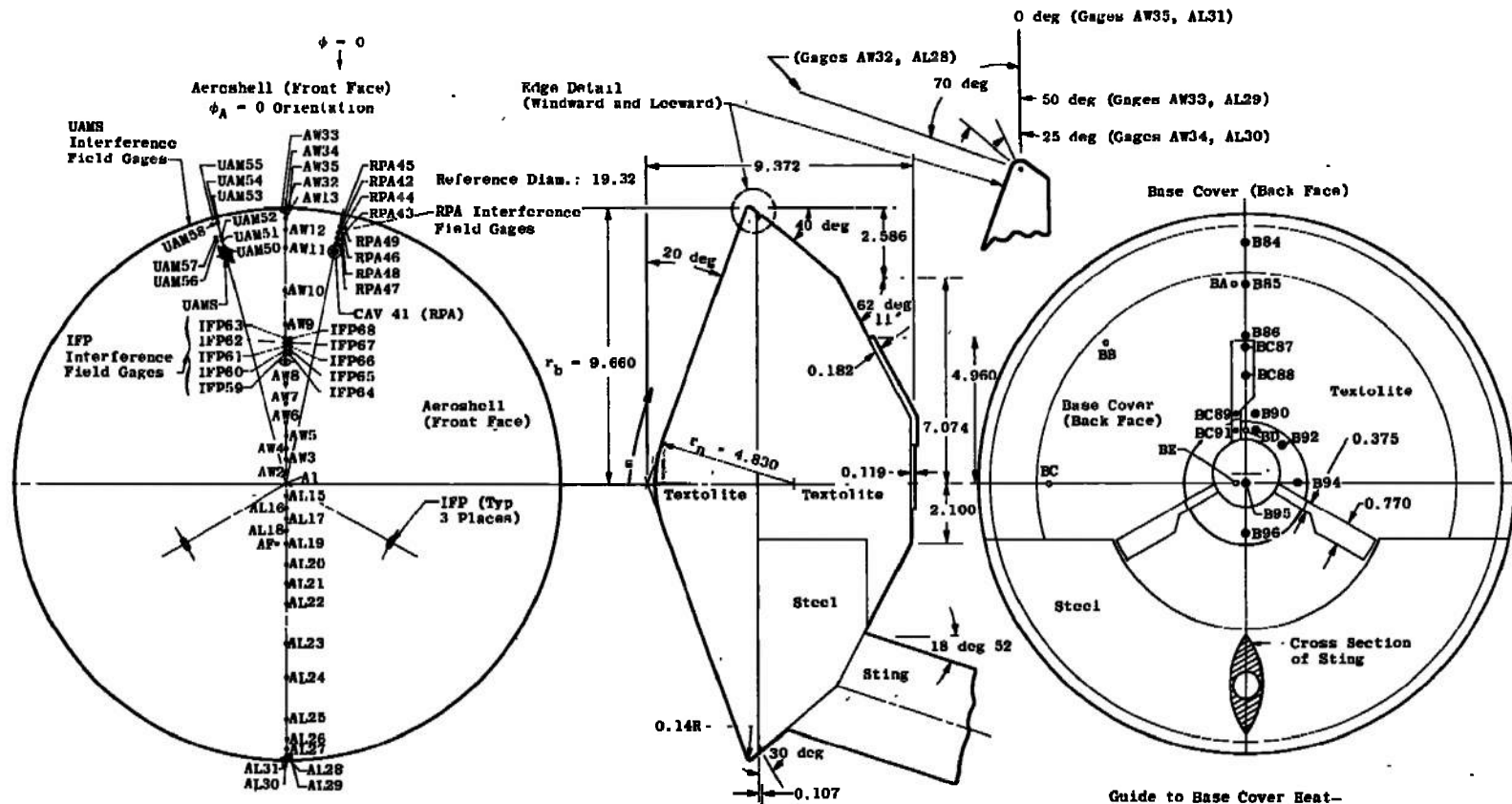
c. Aeroshell surface features



d. Base cover (back face)
Figure 2. Concluded.



PRESSURE AND HEAT-TRANSFER-RATE DISTRIBUTIONS ON A 14-IN.-DIAM HEMISPHERE-CYLINDER MODEL IN TUNNEL F AT $M_\infty \approx 16$ (108-IN.-DIAM TEST SECTION)



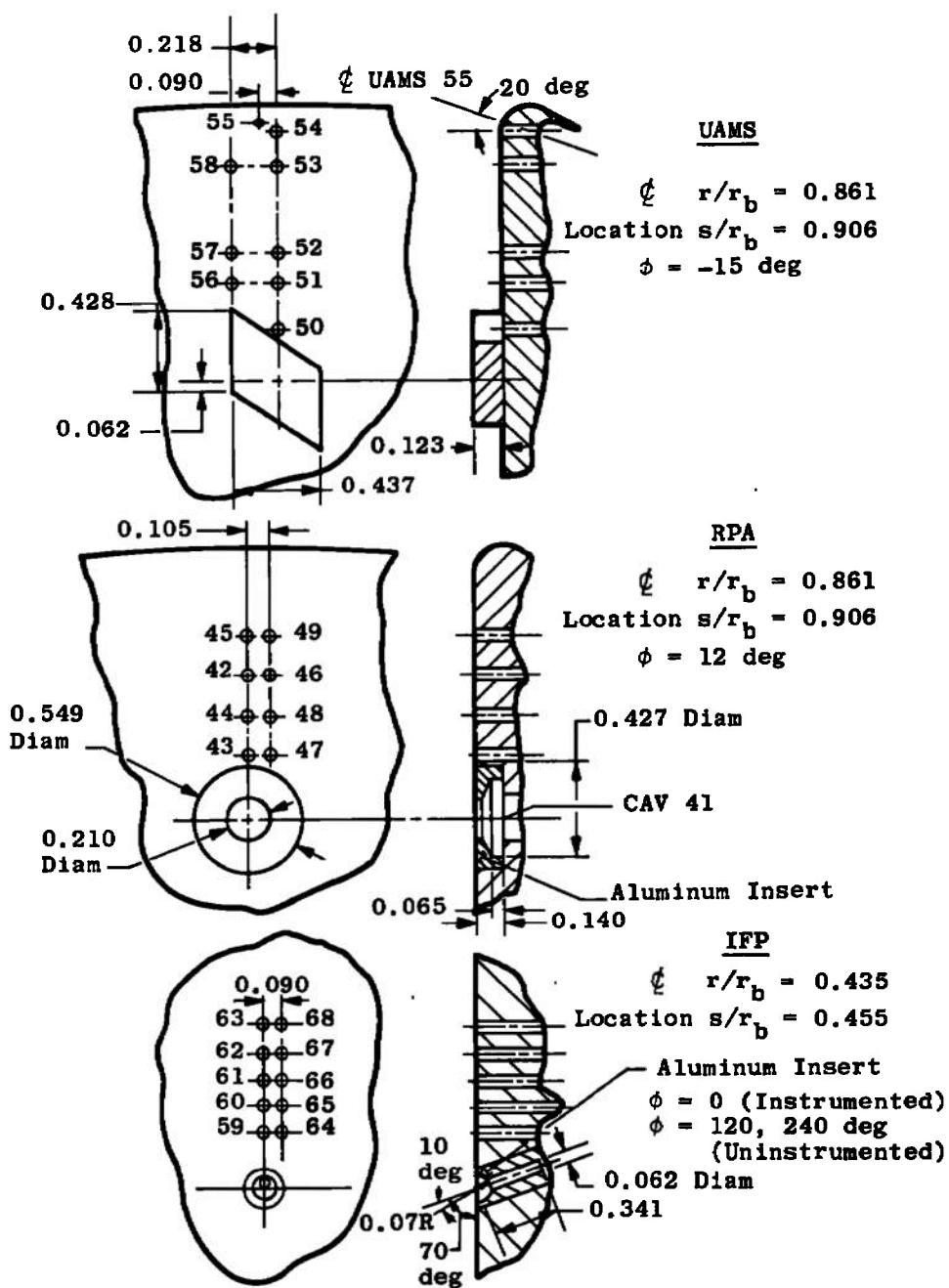
All Dimensions in Inches
 ●● Heat-Transfer Gage
 ○ Pressure Gage

A - Aeroshell (Front Face)
 W - Windward (Upper Side at $\phi = 0$)
 L - Leeward (Lower Side at $\phi = 0$)
 RPA - Retarding Potential Analyzer Interference Field

CAV - RPA Cavity (RT Gage)
 UAM - Upper Atmosphere Mass Spectrometer Interference Field
 IFP - Aeroshell-Bioshield Interface Pad Interference Field

Guide to Base Cover Heat-Transfer and Pressure Gages
 B - Back Face
 BC - Back Face on Bridle Cover

a. Assembly
 Figure 3. Model dimensions and instrumentation.



Notes: All gage numbers prefixed by correspondent surface feature acronym except (CAV) 41.
All dimensions are in inches.

b. Surface features and interference field details
Figure 3. Concluded.

The instrumented portion of the model was constructed of Textolite®, a fiber glass and epoxy laminate. A smooth surface finish was obtained by overlaying the Textolite body with a 0.04-in.-thick layer of Armstrong C-7® epoxy. The lower section of the base cover and the model sting were constructed of stainless steel. Note that the sting was bi-convex in cross section to minimize interference with the model base flow field.

2.3 INSTRUMENTATION

The layout of instrumentation and keys to the gage nomenclature are given in Fig. 3. A complete tabulation of instrument transducer locations is given in Table 1. The aeroshell was instrumented with 61 coaxial thermocouple (COAX) heat-transfer-rate gages and one 15-psid strain-gage pressure transducer. The base cover was instrumented with 13 resistance thermometer (RT) slug-calorimeter heat-transfer gages and five 0.10-psid variable reluctance pressure transducers. One 0.10-psid variable reluctance pressure transducer was mounted at the base of the biconvex model sting to assess possible sting interference effects.

The COAX gages comprise an electrically insulated Chromel® wire enclosed in a cylindrical constantan jacket. A thin-film junction is made between the Chromel and constantan at the model surface. In practical measurement applications, the surface thermocouple behaves as a homogeneous, one-dimensional, semi-infinite solid. The instrument provides an electromotive force directly proportional to surface temperature which may be related by theory to the incident heat flux. The COAX gages are normally used in the range from 3 to 300 Btu/ft² sec. Aeroshell gages 1 through 13 and 15 through 27 were 0.094-in.-diam gages, and gages 28 through 35 and 42 through 63 were 0.063-in.-diam.

Resistance thermometer (RT) slug calorimeter gages use a thin-film platinum resistance thermometer to sense the temperature of an aluminum disk that is exposed to the heat flux to be measured. The calorimeters are fabricated to measure a given range of heat-transfer rate by appropriate selection of the aluminum disk thickness, which in the present case was 0.010 in. giving a range of applicability from 0.05 to 20 Btu/ft² sec. All RT gages on the base cover were 0.250-in. diameter except BC89 and BC91, which were 0.188-in. diameter.

Table 1. Gage and Surface Feature Locations

 $r_n = 4.830$ in. $r_b = 9.660$ in.

Gage Locations						
Heat-Transfer Gage	θ , deg	ϕ , deg	r, in.	s, in.	r/r_b	s/r_b
Aeroshell A1	90	0	0	0	0	0
AW2	85		0.425	0.421	0.044	0.044
AW3	80		0.840	0.843	0.087	0.087
AW4	75		1.250	1.264	0.129	0.131
AW5	70		1.622	1.654	0.168	0.171
AW6			2.100	2.163	0.217	0.224
AW7			2.799	2.908	0.290	0.301
AW8			3.501	3.652	0.362	0.378
AW9			5.601	5.888	0.580	0.610
AW10			6.778	7.141	0.702	0.739
AW11			8.259	8.718	0.855	0.903
AW12			8.973	9.463	0.928	0.980
AW13			9.357	9.874	0.968	1.022
AL15	85	180	0.425	0.421	0.044	0.044
AL16	80		0.830	0.833	0.086	0.086
AL17	75		1.250	1.264	0.129	0.131
AL18	70		1.623	1.655	0.168	0.171
AL19			2.100	2.163	0.217	0.224
AL20			2.799	2.908	0.290	0.301
AL21			3.501	3.652	0.362	0.378
AL22			4.200	4.397	0.435	0.455
AL23			5.601	5.888	0.580	0.609
AL24			6.778	7.141	0.702	0.739
AL25			8.259	8.718	0.855	0.903
AL26			8.964	9.466	0.928	0.980
AL27			9.347	9.874	0.968	1.022
AL28			9.568	10.111	0.991	1.047
AL29	50		9.610	10.160	0.995	1.052
AL30	25		9.647	10.221	0.999	1.058
AL31	0		9.660	10.282	1.000	1.064
AW32	70	0	9.568	10.111	0.991	1.047
AW33	50		9.610	10.160	0.995	1.052
AW34	25		9.647	10.221	0.999	1.058
AW35	0		9.660	10.282	1.000	1.064
RPA Area						
CAV41	70	-12	8.291	8.752	0.858	0.906
RPA42			9.039	9.549	0.936	0.989
RPA43			8.641	9.124	0.895	0.945
RPA44			8.839	9.335	0.915	0.966
RPA45			9.236	9.759	0.956	1.010
RPA46			9.039	9.549	0.936	0.989
RPA47			8.641	9.124	0.895	0.945
RPA48			8.839	9.335	0.915	0.966
RPA49			9.236	9.759	0.956	1.010
UAMS Area						
UAM50		-15	8.535	9.012	0.884	0.933
UAM51			8.803	9.297	0.911	0.962
UAM52			9.068	9.579	0.939	0.992
UAM53			9.390	9.921	0.972	1.027
UAM54			9.583	10.126	0.992	1.048
UAM55	50		9.710	10.160	1.005	1.052
UAM56	70		8.803	9.297	0.911	1.028
UAM57			9.068	9.579	0.939	0.992
UAM58			9.390	9.921	0.972	1.027

Table 1. Concluded.

 $r_n = 4.830$ in. $r_b = 9.880$ in.

Gage Locations							
Heat-Transfer Gage		θ , deg	ϕ , deg	r, in.	s, in.	r/r_b	s/r_b
IFP Area ↓	IFP59	70 ↓	0 ↓	4.459	4.675	0.462	0.484
	IFP60			4.591	4.815	0.475	0.498
	IFP61			4.720	4.952	0.489	0.513
	IFP62			4.852	5.092	0.502	0.527
	IFP63			4.979	5.227	0.515	0.541
	IFP64			4.459	4.675	0.462	0.484
	IFP65			4.591	4.815	0.475	0.498
	IFP66			4.720	4.952	0.489	0.513
	IFP67			4.852	5.092	0.502	0.527
	IFP68			4.979	5.227	0.515	0.541
Back Cover ↓	B84	-40	0 ↓	8.376	---	0.867	---
	B85	-62°10'		6.861	↓	0.710	↓
	B86	-90 ↓		5.101	↓	0.538	↓
	BC87			4.744	↓	0.491	↓
	BC88			3.701	↓	0.383	↓
	BC89			2.390	↓	0.247	↓
	B90			2.390	↓	0.247	↓
	BC91			1.750	↓	0.181	↓
	B92			1.750	↓	0.181	↓
	B93			1.750	↓	0.181	↓
	B94			1.750	↓	0.181	↓
	B95			0	↓	0	↓
	B96	1.750		↓	0.181	↓	
Pressure Gage							
Base Cover ↓	BA	-62°10'	0	6.861	---	0.710	---
	BB	↓	-45	6.861	↓	0.710	↓
	BC	-90 ↓	-90	6.861	↓	0.710	↓
	BD		0	1.750	↓	0.181	↓
	BE		0	0.375	↓	0.039	↓
AeroshellAF		70	+5.9	2.100	2.163	---	0.224
Surface Feature Locations (See Fig. B-3)							
UAMS		70	-15	8.316	8.752	0.861	0.906
IFP		70	12	4.200	4.390	0.435	0.455
RPA		70	0, 120, 240	8.316	8.752	0.816	0.906

The single pressure measurement on the aeroshell was made with a 30-psid semiconductor strain-gage transducer with basic dimensions of 0.6-in. diameter and 0.25-in. thickness. The base cover pressure transducers were variable reluctance gages which are fabricated to

cover a given range of pressures by appropriate selection of the diaphragm material and thickness. The base cover gages were capable of measuring a maximum of 0.1 psid and were of the same basic dimensions as the strain-gage transducer described above.

Tunnel flow conditions were calculated from data on monitor probes (see Fig. 1b) mounted in the test section and from reservoir pressures measured in the arc chamber. The test section measurements were pitot pressure, sensed by two 30-psid strain-gage pressure transducers, and hemisphere stagnation point heat-transfer rates. The heat-transfer rates were inferred from shoulder measurements on 1.0- and 2.0-in.-diam hemisphere-cylinders. The shoulder measurements were obtained from two opposed RT heat-transfer transducers on each cylinder, and the hemisphere stagnation point value was inferred from these measurements. The 1.0- and 2.0-in.-diam stagnation point data were adjusted to correspond to the hemisphere value for a 4.83-in.-radius hemisphere, providing a reference heat-transfer rate for the Viking model. The arc chamber pressure measurement was made with a 40,000-psid semiconductor strain-gage transducer.

The instrumentation described herein was designed and fabricated by AEDC/VKF. Details of transducer design and performance are presented in Refs. 3 and 4.

3.0 PROCEDURE

3.1 TEST CONDITIONS AND PROCEDURES

The data obtained in the present tests were taken at a Mach number of about 16 and Reynolds numbers ranging from 0.5 to 0.9×10^6 , based on model diameter. Test conditions in Tunnel F vary somewhat from run to run and during a tunnel run, as discussed below in Section 3.2. Table 2 lists the tunnel test conditions for one time point per run. These flow conditions correspond to the Viking data presented in this report.

Primary variables of the test program were model angle of attack, α_S , and the aeroshell roll angle, ϕ_A . For two runs (4282 and 4283), the aeroshell surface features were removed to provide "smooth" front-face data. The test matrix is given run by run in Table 3.

Table 2. Summary of Test Conditions

Run	t, msec	p_{∞} , psia	ρ_{∞} , lb _m /ft ³	T_{∞} , °R	U_{∞} , ft/sec	M_{∞}	q_{∞} , psia	Re_d , $\times 10^{-6}$	P_{O_2} , psia	T_{O_2} , °R	H_{O_2} , Btu/lb _m	\dot{q}_{O_2} , Btu/ft ² sec	$P_{O_2}^*$, psia
4266	100	0.004625	0.000116	104.5	7991	15.68	0.796	0.555	5464	4563	1301	24.57	1.480
4267	80	0.005185	0.000143	94.5	7596	15.67	0.892	0.722	5738	4136	1176	22.70	1.656
4268	100	0.004677	0.000139	87.6	7393	15.85	0.822	0.739	5448	3938	1113	20.57	1.526
4269	100	0.004575	0.000120	99.4	7678	15.45	0.764	0.582	4723	4234	1202	21.65	1.420
4270	100	0.004428	0.000110	104.7	7996	15.67	0.761	0.529	5236	4552	1303	24.07	0.418
4271	100	0.003980	0.000150	69.2	6716	16.19	0.730	0.914	4938	3312	918	15.11	1.354
4272	100	0.004858	0.000130	97.6	7655	15.54	0.821	0.639	5162	4204	1194	22.26	1.525
4273	100	0.005059	0.000127	104.3	7757	15.24	0.822	0.591	4806	4315	1227	23.11	1.528
4274	90	0.004377	0.000132	86.3	7396	15.67	0.781	0.712	5379	3911	1114	20.07	1.450
4276	100	0.004638	0.000125	96.6	7602	15.52	0.782	0.620	4876	4155	1178	21.32	1.452
4277	90	0.005124	0.000141	95.2	7567	15.56	0.858	0.701	5402	4113	1167	22.18	1.613
4278	100	0.004248	0.000122	91.1	7517	15.80	0.742	0.631	4982	4067	1151	20.13	1.379
4279	100	0.004137	0.000115	93.8	7693	15.93	0.735	0.592	5240	4238	1205	21.32	1.366
4280	100	0.004524	0.000143	82.3	7152	15.81	0.791	0.782	5050	3713	1042	18.63	1.469
4281	100	0.005026	0.000139	94.4	7550	15.59	0.855	0.698	5364	4096	1162	21.87	1.588
4282	100	0.004478	0.000126	92.8	7585	15.79	0.782	0.647	5259	4130	1172	21.17	1.452
4283	100	0.003868	0.000131	76.9	7200	16.47	0.735	0.772	5696	3765	1054	18.21	1.364
4284	90	0.004895	0.000156	82.1	7143	15.82	0.857	0.850	5434	3700	1039	19.33	1.591

Reference length for Reynolds number, model diameter $d = 19.32$ in.Hemisphere radius, r_p , for $\dot{q}_O = 4.83$ in.

Table 3. Run Schedule

Run	α_s , deg	ϕ_A , deg	α_A , deg	α_{BC} , deg	Comments
4266	0	0	0	0	
4267	-6.0	0	-6.0	-8.0	
4268	-11.2		-11.2	-11.2	
4269	-16.0	0	-16.0	-16.0	
4270	-11.2	0	-11.2	-11.2	
4271	-6.0	0	-6.0	-6.0	
4272	0	180	0	0	
4273	0	180	0	0	
4274	11.2	180	-11.2	11.2	
4276	6.0	180	-6.0	6.0	
4277	11.2	180	-11.2	11.2	Monitor probes removed; tunnel conditions based on $Al(\dot{q}_O)$, $AF(p_{O_2}^*)$ and p_{O_2} .
4278	16.0	180	-16.0	16.0	
4279	18.0	180	-16.0	16.0	
4280	16.0	180	-16.0	16.0	
4281	11.2	180	-11.2	11.2	
4282	11.2	180	-11.2	11.2	Protuberance and recesses smoothed to produce "clean face" data.
4283	16.0	180	-16.0	16.0	
4284	-11.2	0	-11.2	-11.2	Entire front face painted with thermographic phosphor - no transducer data on front face. Monitor probe moved 8 in. forward.

NOTE: Runs 4266-4271, 4282, 4283 made with interference fields gaged; no leeward ray data.

Runs 4272-4281 made with leeward ray gaged; interference field data only on IFP 59-62.

In the conduct of the test, the aeroshell was always run in a flight attitude; that is, the UAMS and RPA surface features were on the "windward" side of the aeroshell. It is recognized that for a very blunt body (front-face cone half-angle, $\theta_c = 70$ deg) such as the Viking, the terms "windward" and "leeward" are somewhat nebulous; however, in application they are the same as for slender bodies. About half of the test was run with the aeroshell roll angle, ϕ_A , at 0, with the remainder being at $\phi_A = 180$ deg. When the aeroshell was rolled 180 deg, the base cover surface features (bridle covers) were in a nonflight orientation with respect to the aeroshell and the wind vector. For this reason, the test matrix lists effective angles of attack for the aeroshell and base cover, as well as the sting angle. All plotted data are denoted by effective angle of attack.

The large number of gaged positions on the model surface precluded running all as active instrumented channels simultaneously. General instrumented regions and corresponding run numbers are noted in Table 3.

The test program was designed to use heat-transfer gages to satisfy the heat-transfer measurement requirements. In addition the thermographic phosphor paint technique was used to supplement the heat-transfer gage results on a second-priority basis. This paint technique is intended to be used to locate "hot spots" on aerodynamic shapes where it is not practical or expedient to instrument with heat-transfer gages. Many tests have been conducted in Tunnel F in the past where useful quantitative paint results were obtained on slender aerodynamic shapes. Because of the large blunt shape of the Viking configuration, the anticipated model bow shock glow occurred and completely eliminated the acquisition of useful paint results on the front face of the model. In combination with an apparent reflectance problem, the strong shock glow eliminated quantitative data acquisition on the back face of the model for all but one run.

For one run at $\alpha_S = -11.2$ deg, the shock glow and reflectance problems were apparently minimal; hence, paint results were deemed acceptable for this run. The paint results indicated no "hot spots" and a consistent trend with the back-face heat-transfer-rate gages.

3.2 DATA ACQUISITION AND REDUCTION

Test data were recorded on a 70-channel digital system capable of scanning all channels in 1 msec and storing up to 150 scans of data.

The data were punched onto paper tape, and basic data reduction was done off-line on a digital computer. As a backup to the digital system, as well as to provide a quick look at the test results, the output of each data channel was recorded on an oscillograph.

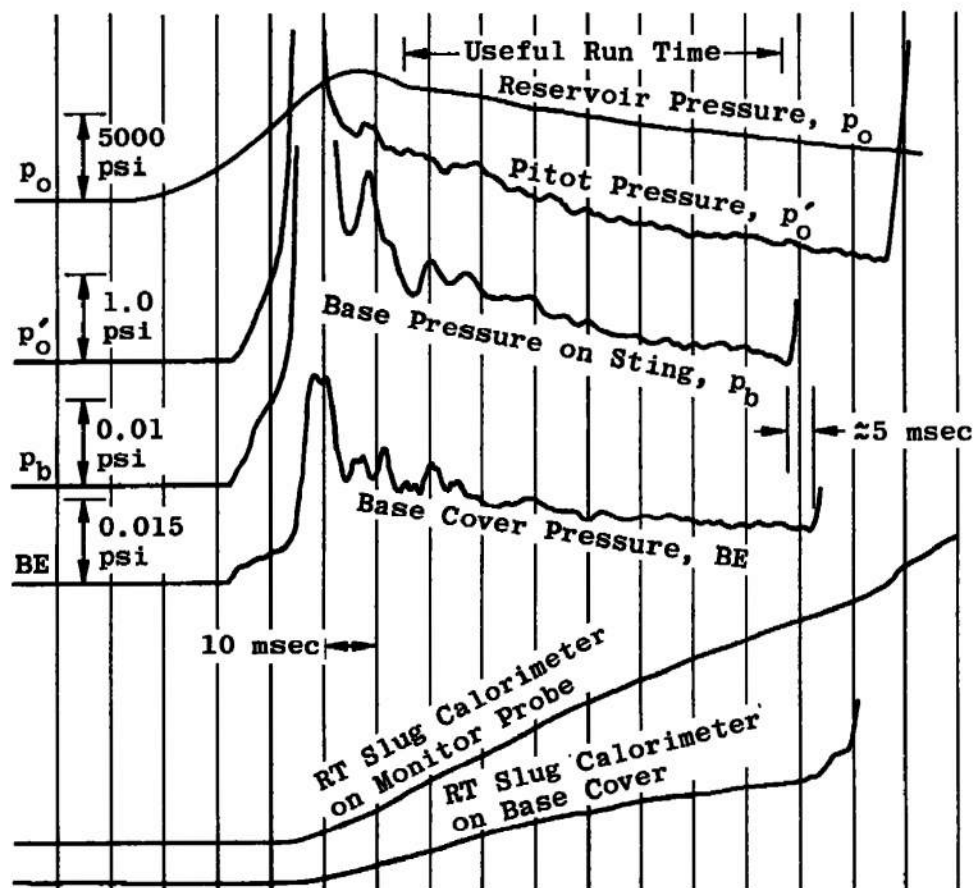
Figure 4 represents examples of the analog traces for the tunnel monitor information (p_o , p'_o , and \dot{q}_o) and for typical model pressure and heat-transfer measurements. Computed digital data obtained from the tunnel monitor inputs is also shown.

Timewise measurements of the test section pitot pressure and hemisphere stagnation point heat-transfer rates were used in conjunction with the Fay-Riddell stagnation point heat-transfer theory (Ref. 5) to infer the reservoir enthalpy. By using this total enthalpy and the measured reservoir and pitot pressures, the test section free-stream conditions were calculated, assuming isentropic flow as described in Ref. 6. A discussion of this method of calculation is presented in Ref. 7.

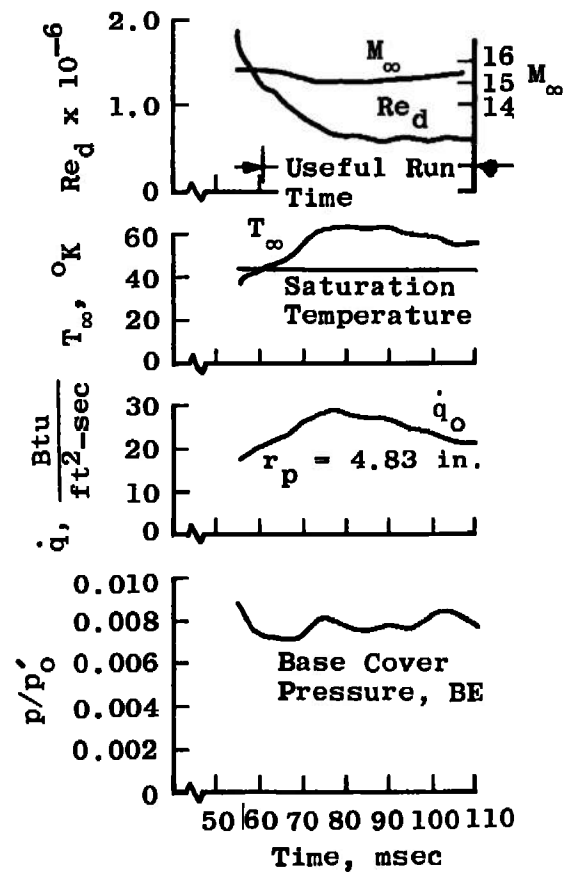
Figure 4b illustrates that while the Mach number remains relatively constant, the free-stream Reynolds number varies significantly. This decrease in Reynolds number with time results from a decreasing reservoir pressure (p_o) and increasing free-stream temperature (T_∞). The first time point for valid model data reduction during a given run is therefore determined by the time at which the free-stream temperature rises to a value at or above the free-stream saturation temperature. This decreasing Reynolds number allows a wide range of Reynolds numbers to be obtained during a single tunnel run.

3.3 DATA PRECISION

The uncertainties in pressure and heat-transfer measurements have been calculated for the present data considering calibration linearity and accuracy, system acquisition accuracies, and uncertainties associated with testing under dynamic conditions. The uncertainties are propagated through the appropriate equations by the Taylor series method of error propagation to yield combined uncertainties. The following table summarizes the uncertainties for the model measurements:



a. Typical analog output



b. Digital data output

Figure 4. Typical timewise variation of tunnel conditions and model data.

<u>Instrumentation Location and Type</u>	<u>Estimated Data Uncertainty, percent</u>
Aeroshell, coaxial thermocouple heat-transfer transducer (\dot{q})	± 9
Base cover, resistance thermometer heat-transfer transducer (\dot{q})	± 9
Aeroshell, strain-gage pressure transducer (p)	± 5
Base cover, variable reluctance pressure transducer (p)	± 5

Specifically excluded from the calculations of uncertainties are flow field dynamic instabilities which appear to be peculiar to blunt-body shapes such as the Viking and which are discussed in Section 4.0 and Appendix A.

The uncertainties associated with the model data reference parameters (p'_0 and \dot{q}_0) were again based primarily on calibration linearity and accuracy, system acquisition accuracy, and uncertainties associated with testing under dynamic conditions. These uncertainties are, as in the case of model measurements, propagated through the appropriate equations by the Taylor series method of error propagation to yield the following estimates of data uncertainty:

<u>Parameter</u>	<u>Uncertainty, percent</u>	<u>Comments</u>
p'_0	± 4	Average of two values
\dot{q}_0	± 5	Average of four values
p_0	± 5	Average of two values
p/p'_0	± 6	
\dot{q}/\dot{q}_0	± 10	

These values were used to estimate uncertainties in the tunnel flow parameters using the Taylor series method of error propagation. Representative parameters are given below:

<u>Uncertainty (\pm), percent</u>								
$\frac{M_\infty}{1.5}$	$\frac{Re_d}{10}$	$\frac{T_\infty}{6}$	$\frac{p_\infty}{6}$	$\frac{T_0}{4}$	$\frac{H_0}{5}$	$\frac{q_\infty}{4}$	$\frac{\rho_\infty}{8}$	$\frac{U_\infty}{3}$

The model attitude position was set prior to each run, and the pitch and roll angles are estimated to be accurate within ± 0.10 deg.

The estimated uncertainty for the sting base pressure measurement is ± 10 percent.

4.0 SUMMARY OF RESULTS

The data presented in this summary were obtained for Reynolds numbers, Re_d , from 0.5×10^6 to 0.9×10^6 . Reynolds numbers and Mach numbers are identified on each figure, and the complete listing of flow parameters is given in Table 2.

One of the chief concerns of the model installation was the influence of the monitor probe shock wave on the model base flow (see Fig. 1b). At model angles of attack from $\alpha_s = 16$ deg, the knife-edged sting was intercepted by the probe shock. In order to monitor possible effects, if any, of this shock-sting interaction on the model base flow and its duration, a pressure transducer was mounted on the sting at the point where guy wires were attached (see illustration in Fig. 5). When the model was pitched positive ($\alpha_s > 0$), the sting was lowered and interacted with the probe shock. Despite this, the pressures (p_b) measured on the sting were near the value of those on the base cover as shown in Fig. 5; removing the monitor probe produced no change in the sting base pressure level or the model base cover pressures. As the model was pitched negative, the sting moved upward and away from the influence of the probe shock; however, the sting base pressure increased to about three times the base cover level. There was no increase in model base cover pressures when the sting base pressure increased at the negative angles. The base pressure transducer was mounted on the top of the sting, which meant that its position was "leeward" for positive angle of attack and "windward" for negative angles. The "windward" positioning may have caused the increase in pressure at negative angles.

The Viking model presented some special problems in testing because of its size and bluntness. Because of the electric-arc method of test gas heating, some contamination of the test gas with solid particles was inevitable; and the Viking model with about 300 in² of front surface area was particularly susceptible to particle impingement. In general, 3 to 5 particles were observed in the front-face gage data and/or schlieren movies during the useful time of each run.

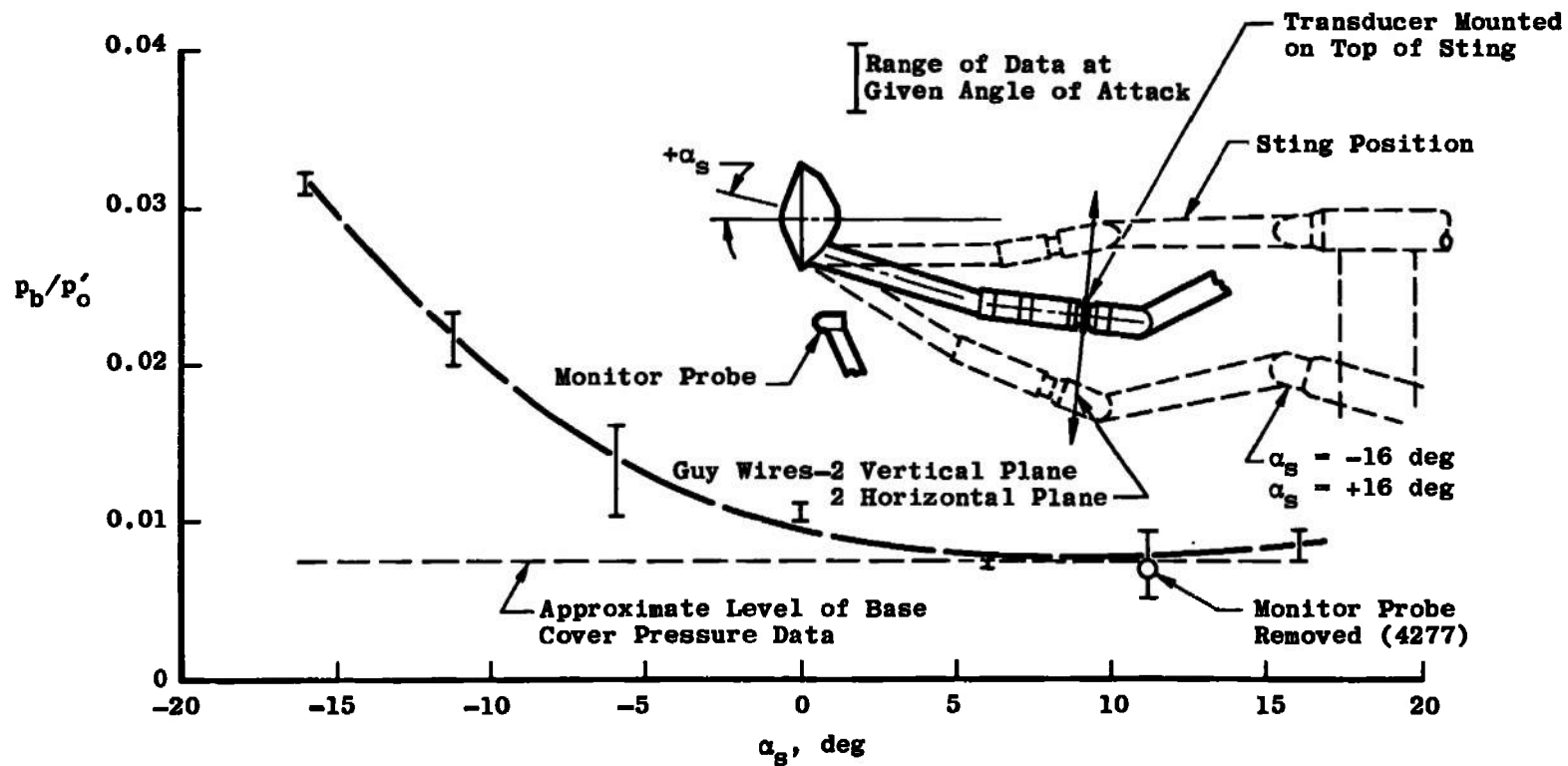


Figure 5. Summary of base pressure data.

The influence of particle impingement and rebound caused a shock disturbance and consequently an erratic behavior pattern in the heat-transfer output in the vicinity of the impact area; a typical example is shown in Fig. 6. The disturbance shown on the figure has a duration of about 8 msec; however, its influence on the calculated heat-transfer rate extends for an additional 20 msec because of the 21-point central difference formula used to smooth the raw data trace. In obtaining useful data from such disturbances, fairings were drawn excluding the disturbance effect, as shown in Fig. 6. The back-face data were not noticeably affected by particle disturbances.

A given particle did not necessarily affect all gages being monitored on a given run; therefore, the extent of influence of a disturbance on the model face gage data varied with the apparent size of the particle and the point of impact. Table 4 lists the number of gages that were corrected for particle influences for each run.

To monitor the pressure level on the model front face, a single pressure tap (AF) was located at $s/r_b = 0.224$ (s is the surface distance on model at zero-incidence stagnation point and r_b is the base radius of the Viking model). The data for this tap are summarized in Fig. 7 where a comparison is made with a theoretical blunt-body pressure distribution determined using the method of South (Ref. 8) corrected for angle of attack by Newtonian impact theory. The agreement is seen as generally good.

The aeroshell (front-face) heat-transfer-rate data in ratio form are presented in Fig. 8. At $\alpha_A = 0$, a comparison is made with theoretical data calculated by the method of Patankar and Spalding (Ref. 9) as applied by Mayne and Dyer (Ref. 10) using the pressure distribution obtained from the South blunt-body program (Ref. 8). At the three angles of attack tested ($\alpha_A = -6, -11.2$, and -16) there was a large amount of scatter in the windward ray data, while the leeward ray data were quite smooth and consistent. The data scatter is particularly evident for the case of $\alpha_A = -11.2$ deg, the vehicle trim angle. The heat-transfer instrumentation would be expected to yield results similar to those observed on the leeward side of the aeroshell surface, as shown in Fig. 8. The nonrepeatability of measurements on the windward side of the aeroshell is, therefore, attributed not to instrumentation inaccuracies, but rather to a nonrepeatable aerodynamic process. Analysis and discussion of possible sources of the scatter are given in Appendix A.

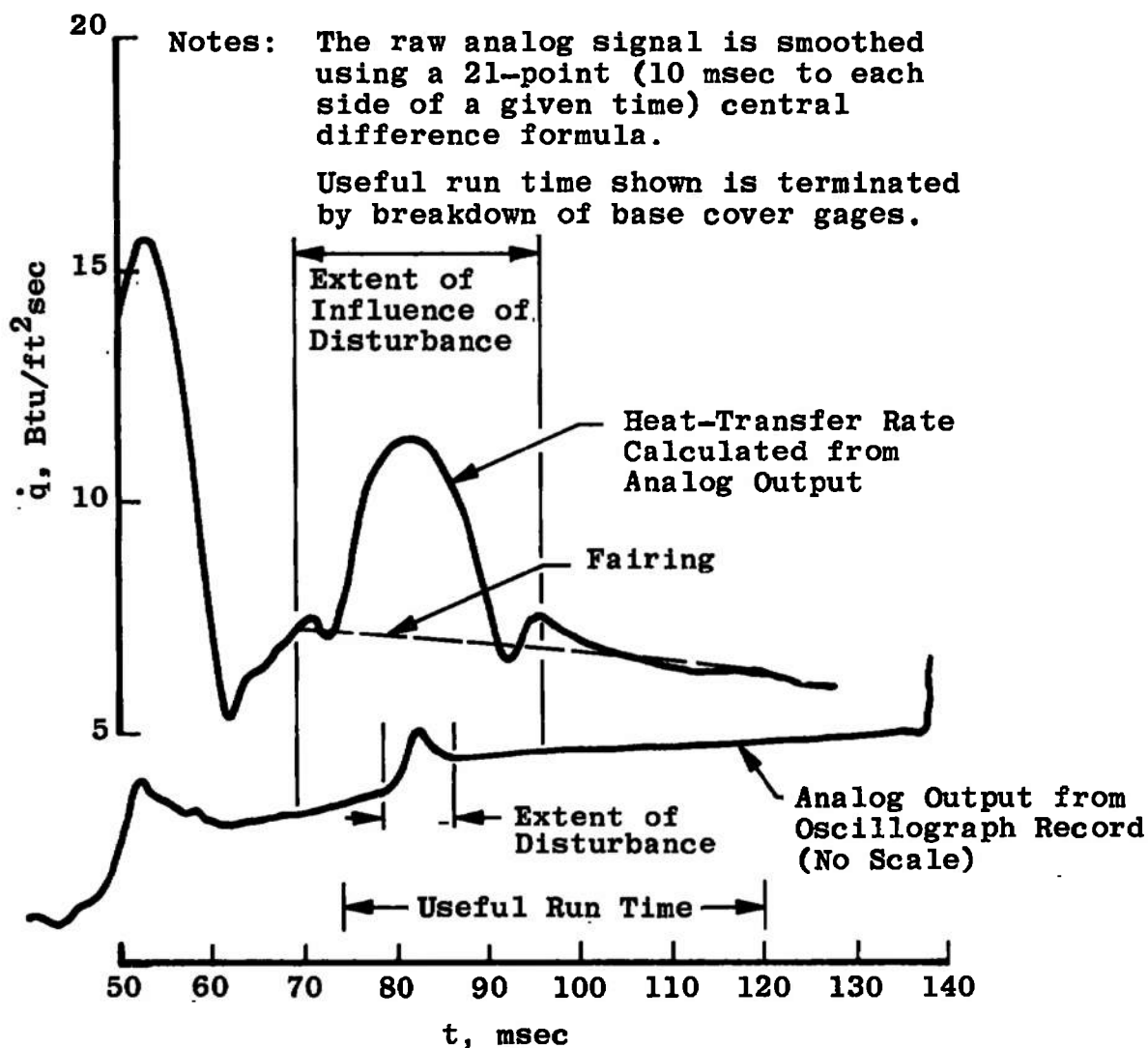


Figure 6. Comparison of analog signal with calculated heat-transfer rate-coaxial thermocouple transducer.

Table 4. Number of Gages Corrected by Fairing
for Particle Influences on a Given Run

Run	Number of Front-Face Gages Corrected
4266	27
4267	22
4268	16
4269	8
4270	7
4271	6
4272	26
4273	2
4274	3
4276	18
4277	23
4278	9
4279	22
4280	23
4281	28
4282	14
4283	19

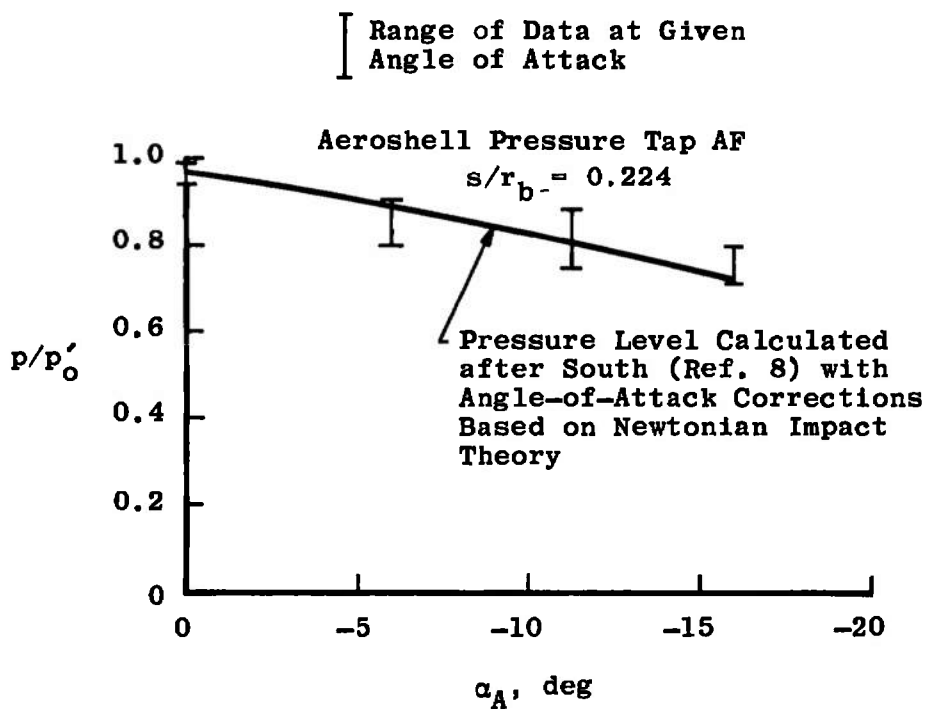
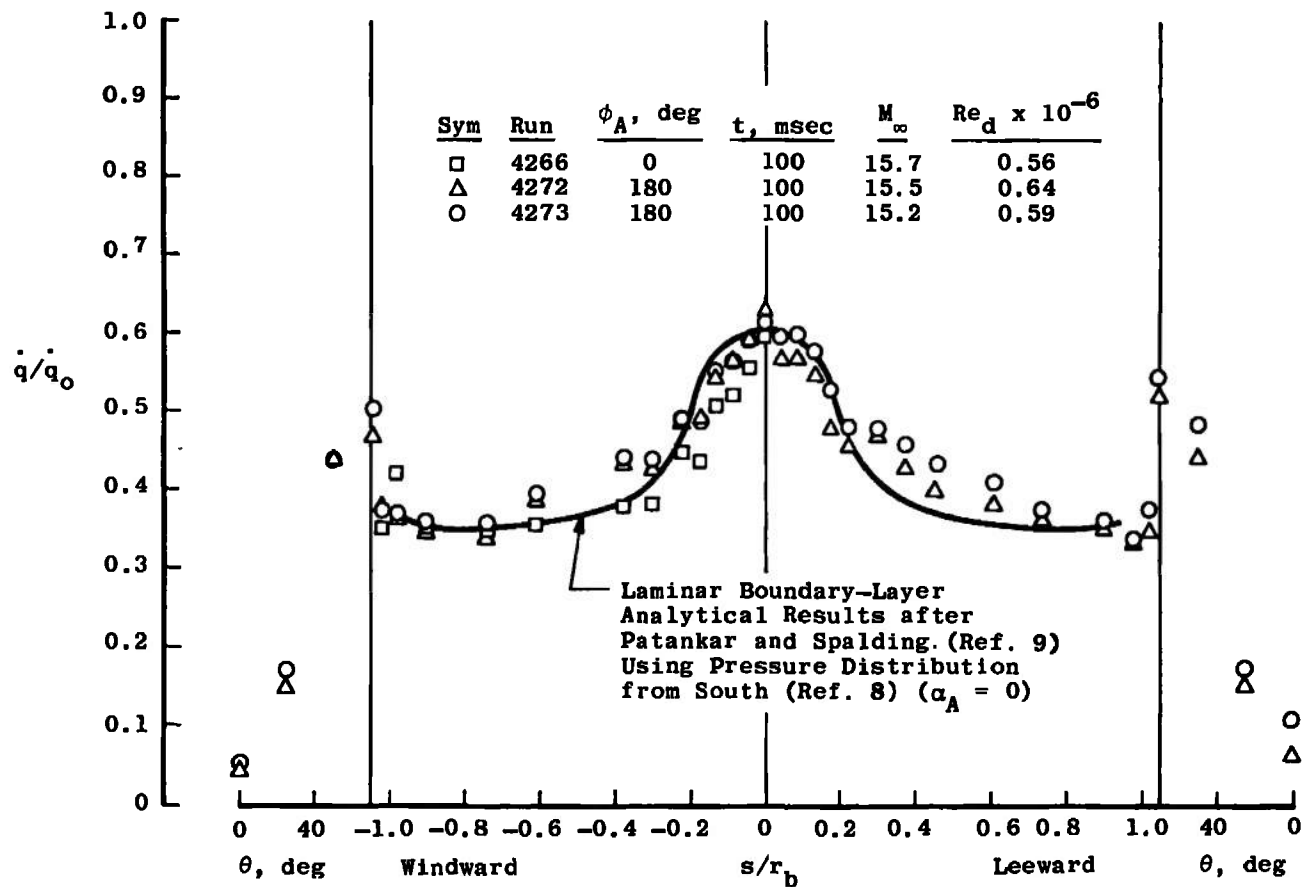
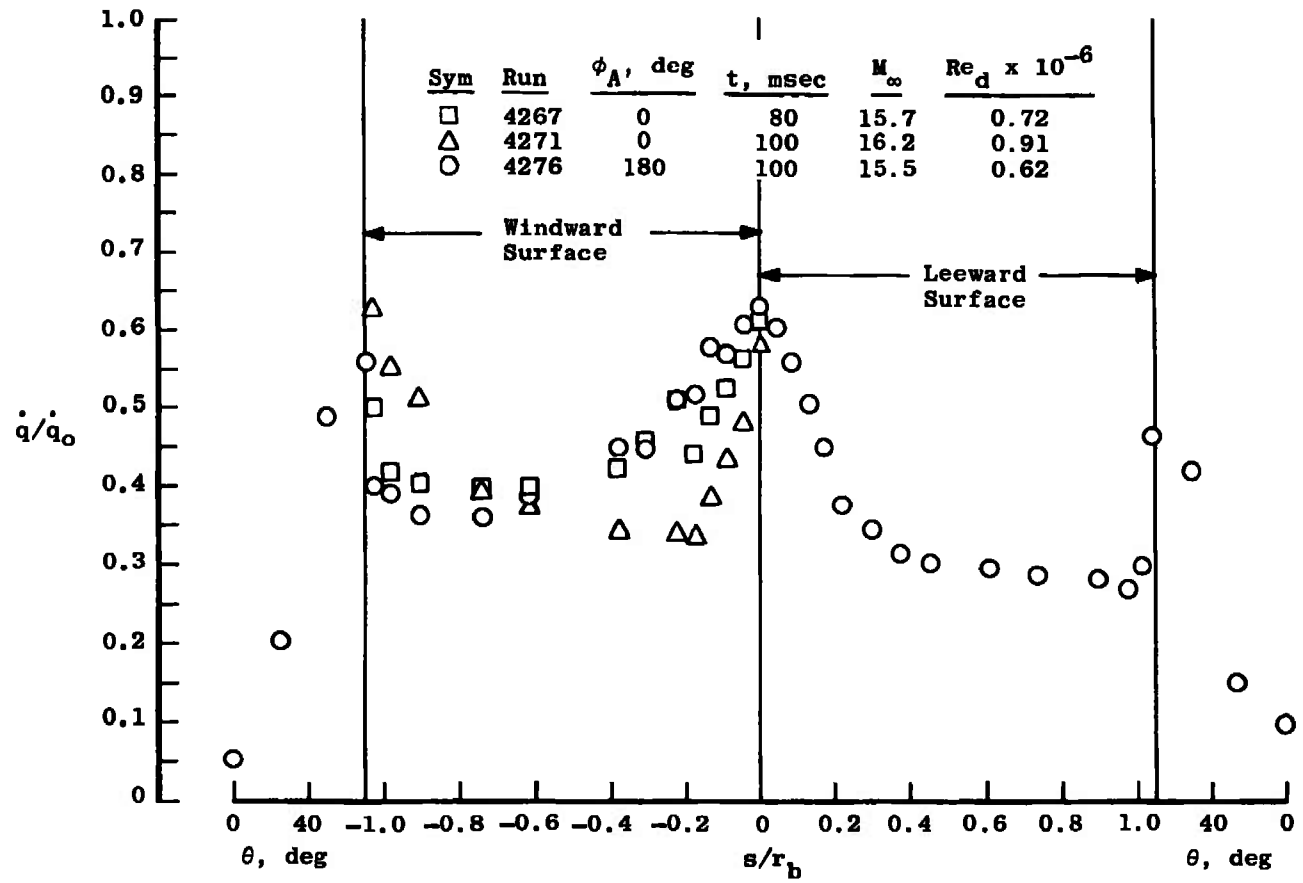


Figure 7. Summary of aeroshell (front face) pressure data.

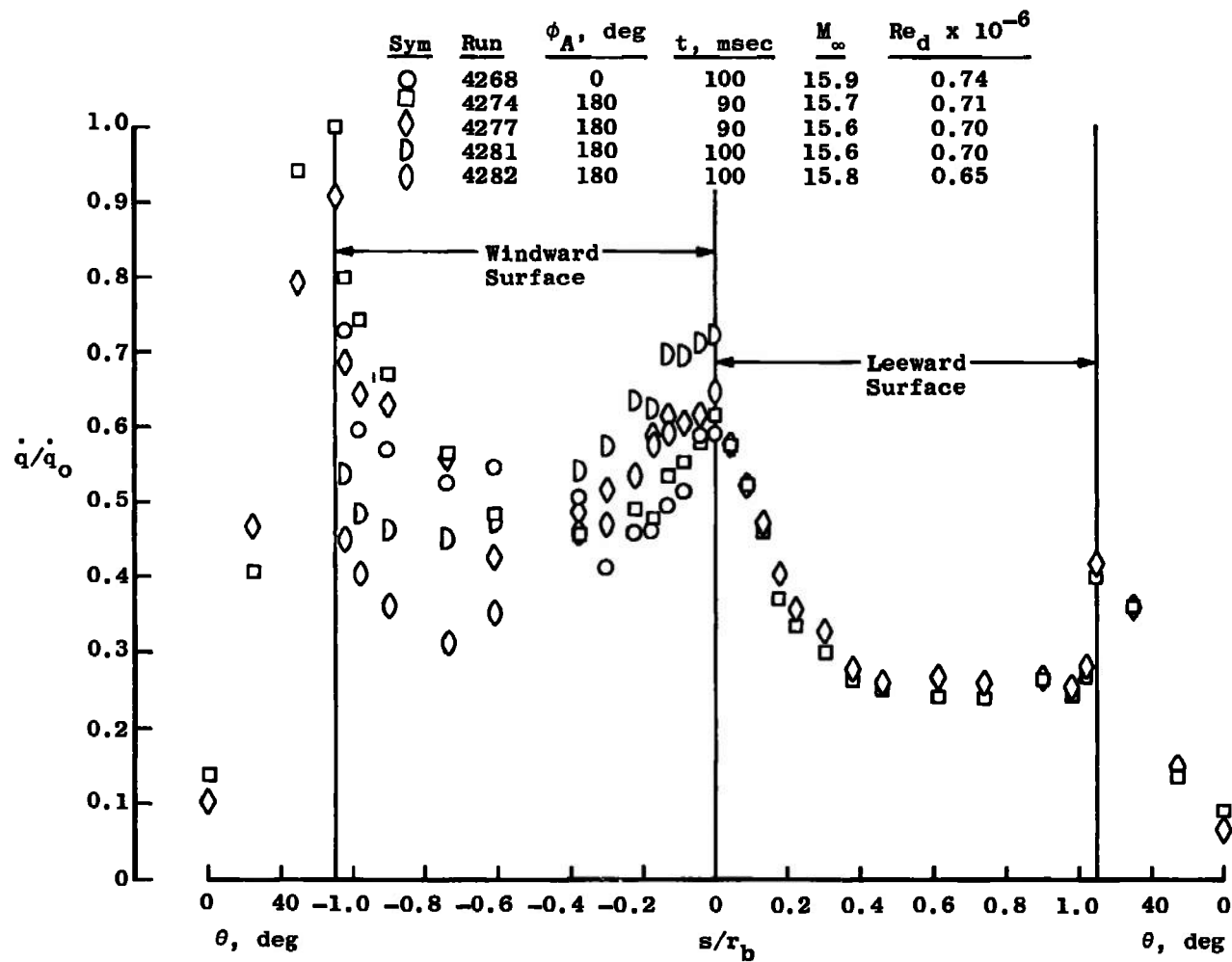


a. $\alpha_A = 0$ deg

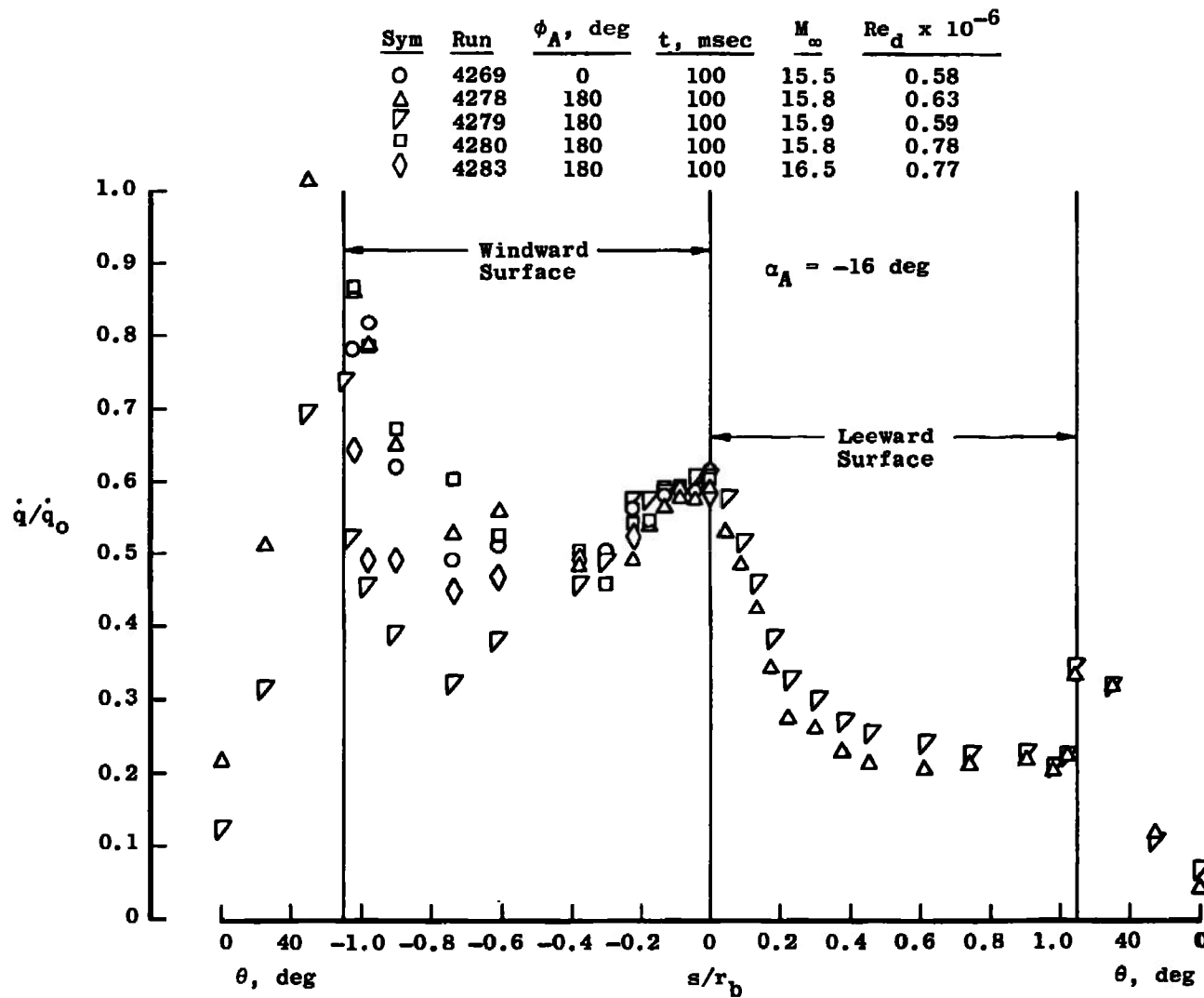
Figure 8. Summary of aeroshell (front-face) heat-transfer-rate data.



b. $\alpha_A = -6.0$ deg
Figure 8. Continued.



c. $\alpha_A = -11.2$ deg
Figure 8. Continued.



d. $\alpha_A = -16.0$ deg
Figure 8. Concluded.

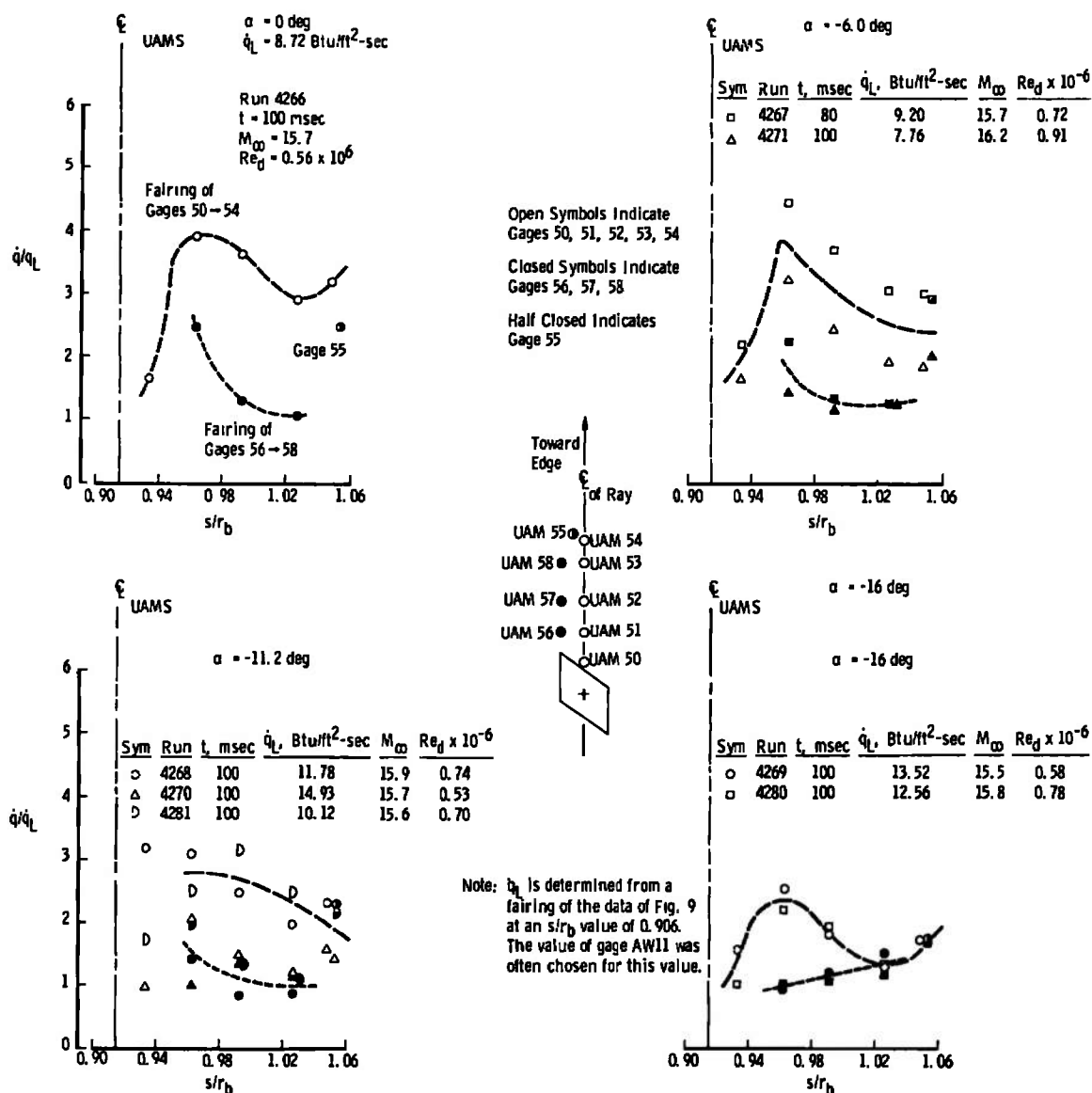
Heat-transfer-rate data from the UAMS interference field gages are presented in Fig. 9a. The measured to local heat-transfer ratio, \dot{q}/\dot{q}_L , is used in the analysis of the interference field data. The value of \dot{q}_L represents the value of heat-transfer rate at the s/r_b value of the disturbance on the $\phi = 0$ streamline. This value was determined from a fairing of the data shown in Fig. 8 at an s/r_b value of 0.906. Often the fairing indicated that the value of AW11 ($s/r_b = 0.9025$) was appropriate for \dot{q}_L . Using this ratio, a value of unity should be expected for the case of noninterference only in the immediate area of the protuberance.

A considerable difference is noted at all angles of attack between the two rows of gages. The ratio \dot{q}/\dot{q}_L tends toward unity as the edge of the model is approached for the outer row of gages (56 \rightarrow 58) at $\alpha_A = 0, -6$, and -11.2 deg. The centerline row of gages show \dot{q}/\dot{q}_L significantly above unity all the way to the edge of the model.

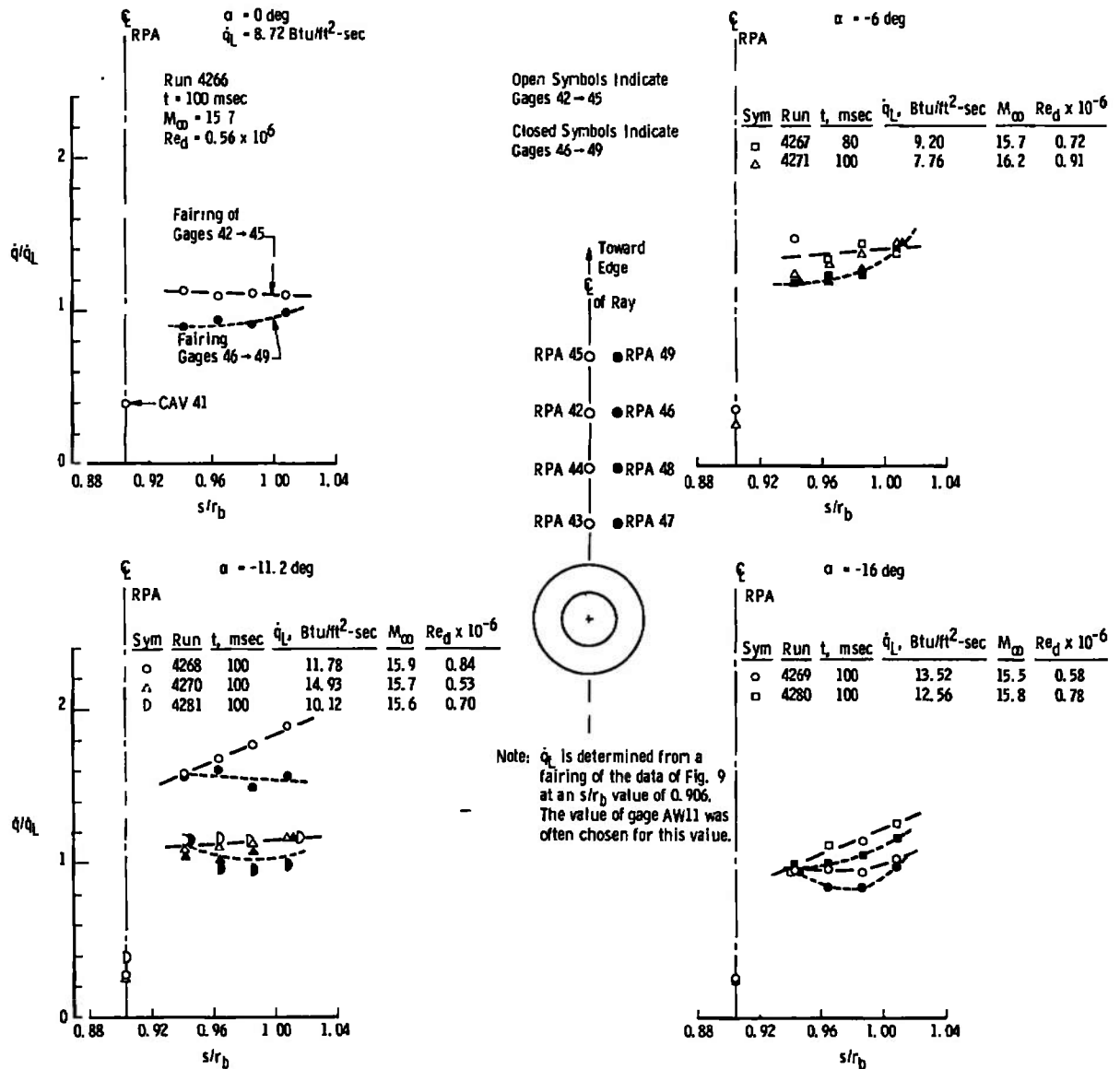
The RPA interference field data are shown in Fig. 9b. Since the RPA is located at the same s/r_b station as the UAMS (see Fig. 3), the same values of \dot{q}_L are applicable. Here again the field of gages consists of two rows. The data from the row in line with the RPA generally average 10 percent above the row which is off centerline. The maximum values are significantly lower than those experienced in the UAMS field.

The (IFP) interference field data are presented in Fig. 9c. As with the UAMS and RPA interference data, the parameter \dot{q}/\dot{q}_L is used. In this case, \dot{q}_L is determined from a fairing of the data of Fig. 8 at an s/r_b of 0.455. Again in this case the interference field consists of two rows of gages, one of which is on a ray through the centerline of the disturbance. The data of Fig. 9c show essentially a flat distribution with an average value of \dot{q}/\dot{q}_L around unity. There is no apparent trend in these data of the centerline row of gages being higher than the off-centerline row, as was evident with the UAMS and the RPA.

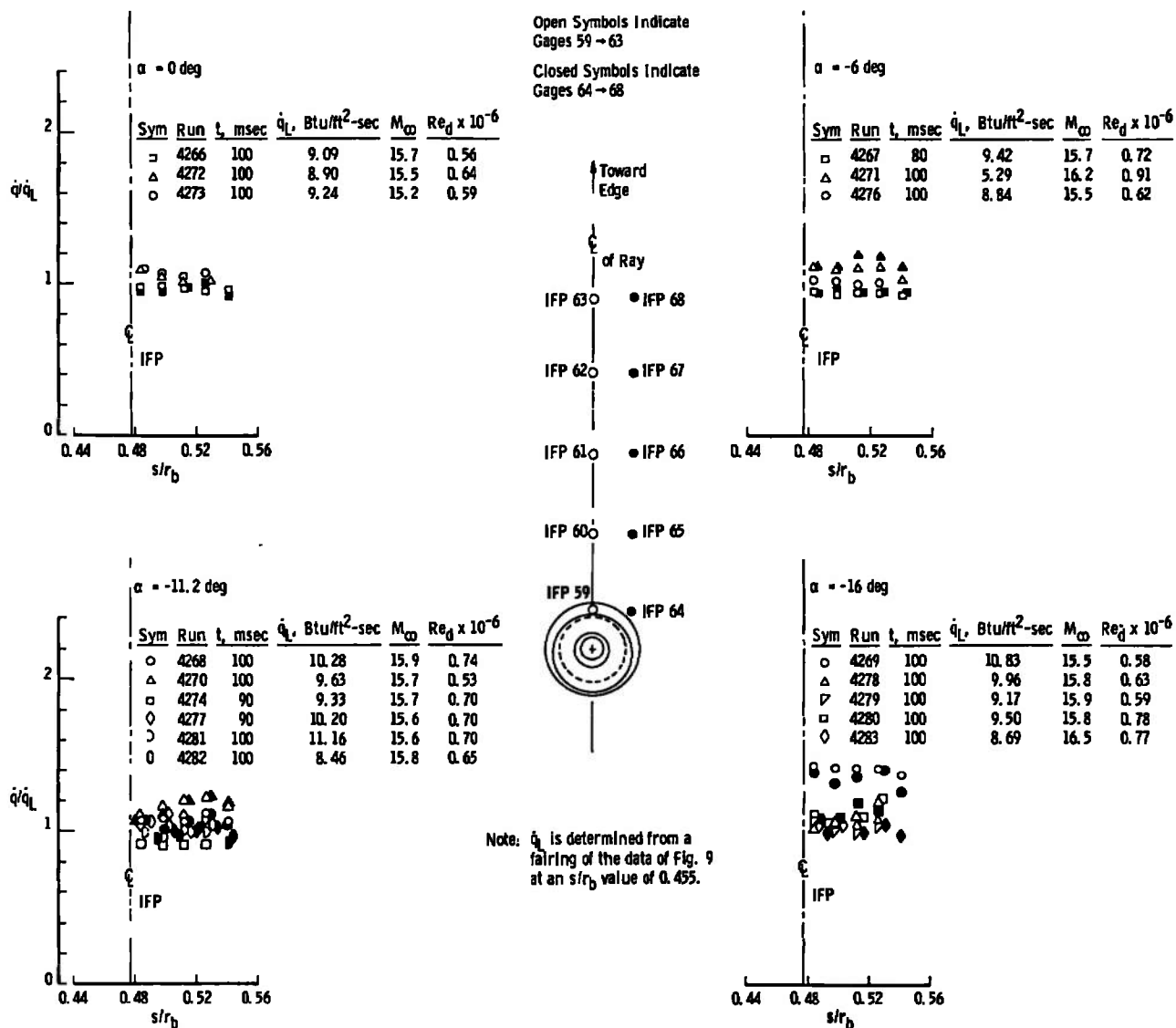
Data obtained on the base cover are summarized in Fig. 10. At zero pitch, there is a peak in the heating rate near $r/r_b = 0.2$, and for negative angles of attack (flight orientation) the profile becomes quite flat as angle of attack is increased. For positive angles, however, a sharp peak is observed near the outer edge of the model. The maximum measured peak heating rate was 2.5 percent of the reference value.



a. UAMS interference field
 Figure 9. Heat-transfer-rate data.



b. RPA interference field
 Figure 9. Continued.



c. IFP interference field
Figure 9. Concluded.

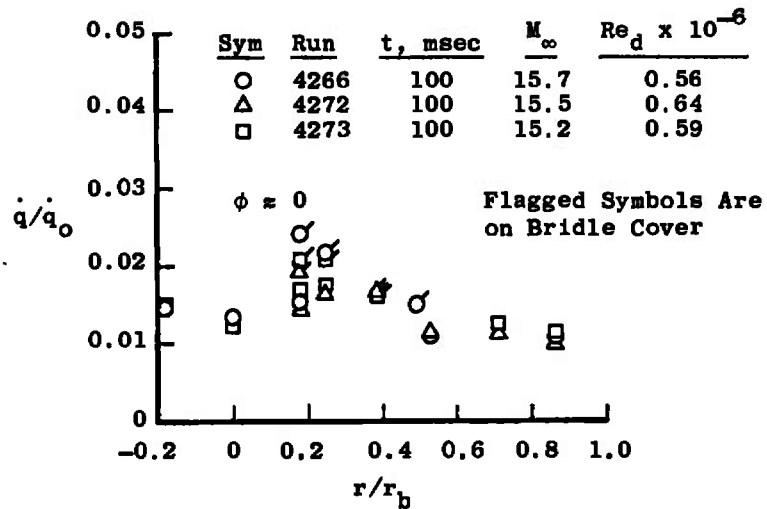
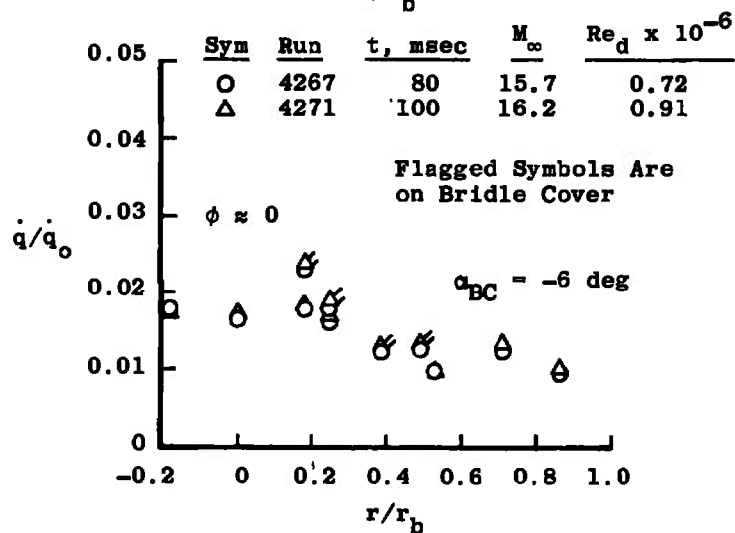
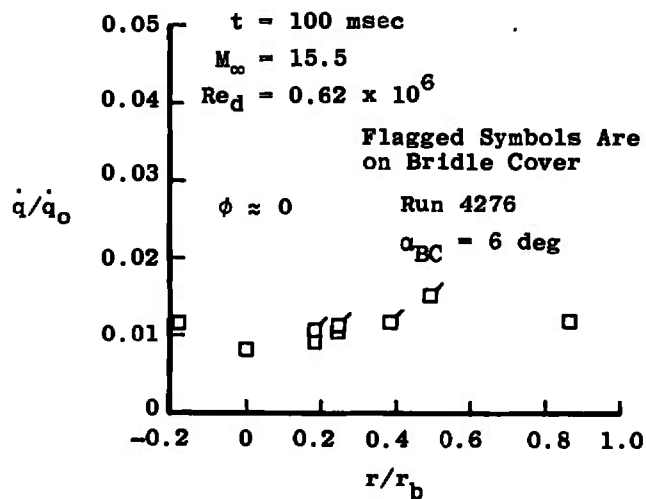
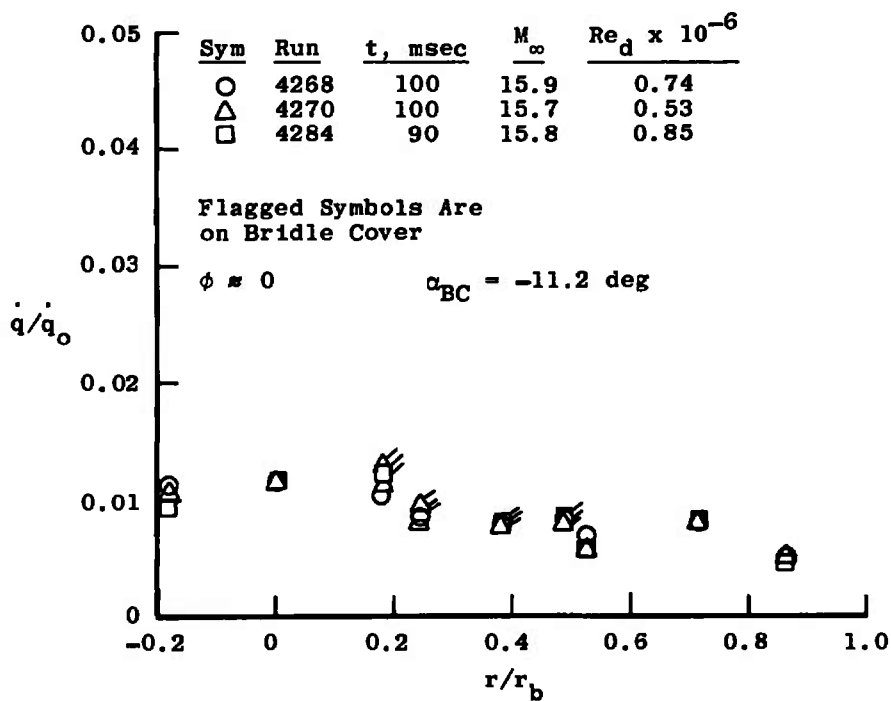
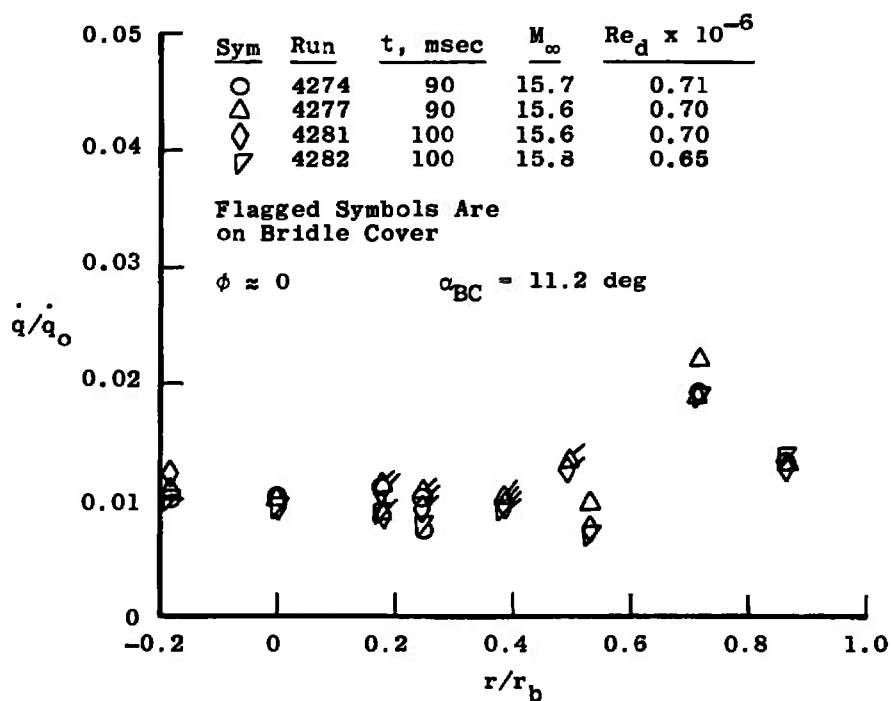
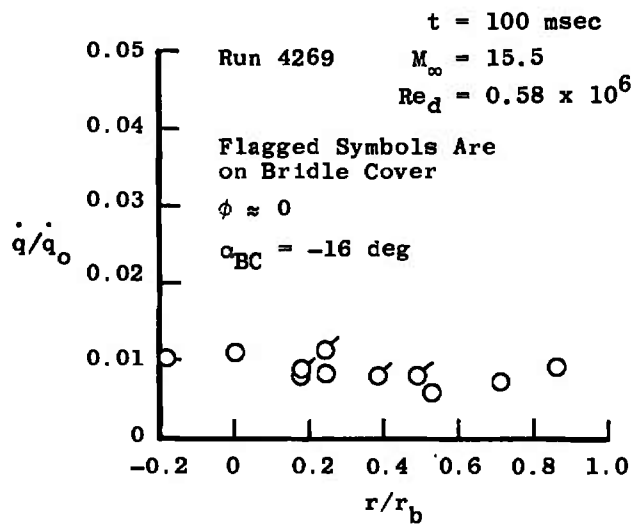
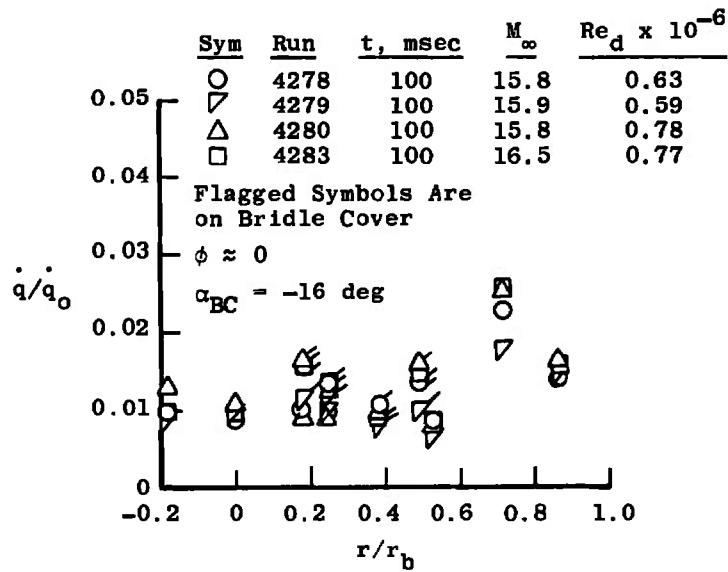
a. $\alpha_{BC} = 0 \text{ deg}$ b. $\alpha_{BC} = \pm 6 \text{ deg}$

Figure 10. Summary of base cover heat-transfer-rate data.



c. $\alpha_{BC} = \pm 11.2$ deg
Figure 10. Continued.



d. $\alpha_{BC} = \pm 16 \text{ deg}$
Figure 10. Concluded.

5.0 CONCLUDING REMARKS

The following conclusions can be drawn from the laminar boundary-layer heat-transfer-rate data obtained on the Viking Entry Vehicle model at $M_\infty \approx 16$ and $Re_d \approx 0.6 \times 10^6$ to 0.9×10^6 :

1. Stagnation point heat-transfer rates are about 60 percent of the value of a hemisphere having the same radius as the Viking nose.
2. The data indicate heat-transfer rates can rise to the hemisphere stagnation value near the edge of the aeroshell (windward surface).
3. Maximum peak heating rates on the base cover (back face) did not exceed 2.5 percent of the hemisphere stagnation value.
4. Interference heating amplification of local heat transfer does occur downstream of the surface features. The protruding UAMS cover produced amplifications of four times the local value, and the RPA cavity produced changes up to a factor of about 2. Interference heating from the IFP proturbance did not exceed an amplification factor of 1.4.
5. Erratic timewise and run-to-run nonrepeatability of the most windward aeroshell heat-transfer-rate data which occurred has been attributed to very small spatial and timewise variations that can occur in the tunnel free-stream flow. Theoretical calculations have provided supporting evidence that extremely small variations in tunnel flow properties are sufficient to significantly affect the surface data on very blunt bodies having sonic corners. The magnitude of these flow field disturbances is small enough to be well within the quoted uncertainties for the facility and well within the tunnel flow properties that can be calibrated and defined.

REFERENCES

1. Hunt, James L. and Jones, Robert A. "Effects of Several Ramp-Fairing, Umbilical, and Pad Configurations on Aerodynamic Heating of Apollo Command Module at Mach 8." NASA TM X-1640, September 1968.
2. Eaves, R. H., Jr., Griffith, B. J. and Buchanan, T. D. "Design and Initial Calibration of the AEDC-VKF Tunnel F with an Enlarged Arc Chamber." AEDC-TR-69-122 (AD862975), December 1969.
3. Ledford, R. L., Smotherman, W. E. and Kidd, C. T. "Recent Developments in Heat-Transfer-Rate Pressure and Force Measurements for Hotshot Tunnels." AEDC-TR-66-228 (AD645764), January 1967.
4. Bynum, D. S. "Instrumentation for the AEDC/VKF 100-In. Hotshot (Tunnel F)." AEDC-TR-66-209 (AD804567), January 1967.
5. Fay, J. A. and Riddell, F. R. "Theory of Stagnation Point Heat Transfer in Dissociated Air." Journal of Aeronautical Sciences, Vol. 25, No. 2, February 1958, pp. 73-85, 121.
6. Grabau, Martin, Smithson, H. K., Jr., and Little, Wanda J. "A Data Reduction Program for Hotshot Tunnels Based on the Fay-Riddell Heat-Transfer Rate Using Nitrogen at Stagnation Temperatures from 1500°K to 5000°K." AEDC-TDR-64-50 (AD601070), June 1964.
7. Griffith, B. J. and Lewis, Clark H. "Laminar Heat Transfer to Spherically Blunted Cones at Hypersonic Conditions." AIAA Journal, Vol. 2, No. 3, March 1964, pp. 438-444.
8. South, Jerry C., Jr. "Calculation of Axisymmetric Supersonic Flow Past Blunt Bodies with Sonic Corners, Including a Program Description and Listing." NASA TN D-4563, 1968.
9. Patankar, S. V. and Spalding, D. B. Heat and Mass Transfer in Boundary Layers. CRC Press, Cleveland, Ohio, 1968.

10. Mayne, A. W., Jr. and Dyer, D. F. "Comparisons of Theory and Experiment for Turbulent Boundary Layers on Simple Shapes at Hypersonic Conditions." Proceedings of the 1970 Heat Transfer and Fluid Mechanics Institute, Stanford University Press, 1970, pp. 168-188.
11. Barnwell, R. W. "A Time-Dependent Method for Calculating Supersonic Blunt-Body Flow Fields with Sharp Corners and Embedded Shock Waves." NASA TN D-6031, 1970.

APPENDIX A

EVALUATION OF SHOCK SHAPES AND FLOW-FIELD
NONUNIFORMITIES

The problem of unusually large data scatter on the windward surface of the aeroshell was discussed in Section 4.0 and illustrated in Fig. 8. Analysis of the test data revealed phenomena which may be associated with the data scatter. These three possibilities are (1) shock oscillations on the windward surface, (2) p_0 profile and shock shape nonuniformity along the windward surface, and (3) nonuniform local flow-field effects on the windward surface heat-transfer rate.

Shock Oscillations

The first observation is illustrated in Fig. A-1, where examples of the analog heat-transfer-rate signals are shown for the four angles of attack tested. It can be seen that the aeroshell (front-face) windward data traces show high-frequency oscillations which become more prevalent as the angle of attack is increased. Though the amplitude of the oscillations is small, the effects on the reduced heat-transfer-rate data can be a much larger percentage of the total value (as shown previously in Fig. 6).

During the test, high-speed schlieren motion pictures (≈ 4000 frames/sec) were obtained which showed that the bow shock was unsteady even in the absence of the particle disturbances discussed earlier in Section 4.0. The motion-picture film was read to obtain shock locations at nine positions on the aeroshell ($r = 0, \pm 2, \pm 4, \pm 6, \pm 8$ in.), with up to 160 frames being read on a given run. The data are illustrated in Fig. A-2 for three body positions from Run 4274. The oscillations shown are on the order of two per millisecond. The frequency of the shock oscillation is much higher than the frequency shown for the windward heat-transfer-rate data (Fig. A-1). There is also no obvious difference between windward and leeward shock position data. Based on the heat-transfer results shown in Fig. 8a and hemisphere-cylinder results to be presented in this Appendix, it appears that the shock oscillations did not produce the heat-gage output oscillations as confirmed by the $\alpha_A = 0$ deg data and the relative absence of any significant data scatter. On the other hand, the effect of shock oscillations at angle of attack on the windward surface heat-transfer rates might be significant.

p_0 Profiles and Shock Shapes

Fairings of the shock position data at one time point per run are shown in Fig. A-3 at a radial location of $r = -8$ on the windward surface. Note the distinct difference between the $\phi_A = 0$ data and the $\phi_A = 180$ deg data at all angles of attack. A crossplot of Fig. A-3 and eight similar plots at the other radial locations yields a graphical representation of the bow shock, as shown in Fig. A-4. Figure A-4a shows the difference in shock shape due to the roll angle, ϕ_A , of the aeroshell. If spatial nonuniformities in the tunnel flow cause this difference, the shock standoff should be essentially the same if these data are replotted in terms of tunnel orientation instead of model orientation. Note that when model orientation is used the windward half of the aeroshell is in the top half of the tunnel for $\phi_A = 0$ and in the bottom half of the tunnel for $\phi_A = 180$ deg. This can, of course, only be done at $\alpha_S = 0$. (Note: Normally the $-r$ values are windward and $+r$ values are leeward.) Plotting in tunnel orientation as shown in Fig. A-4b clearly illustrates that the differences in shock standoff as shown in Fig. A-4a are due to the windward surface ($-r$ locations) being in the top of the tunnel for $\phi_A = 0$ and in the bottom of the tunnel for $\phi_A = 180$ deg. Figure A-4c shows that a difference does exist in the tunnel pitot pressure level between the top and bottom of the tunnel. Figure A-5 gives examples at other angles of attack and clearly shows this difference in shock shape due to aeroshell roll angle.

If there is a direct correlation between shock shape and the heat-transfer data on the windward surface, one may assume that two runs with disparate heat-transfer-rate distributions would have different shock locations. This assumption was checked by comparing two runs at the same ϕ_A angle which have substantially different heat-transfer levels on the windward surfaces. Windward surfaces results shown in Fig. 8c at $\alpha_A = -11.2$ deg for Runs 4274 and 4282 are excellent examples. One should expect a significant difference in shock shape if this hypothesis is correct. Figure A-3 shows this is indeed the case for these two runs ($r = -8$ shown here, all radial locations checked). Hence, the scatter on the windward surface in Figs. 8b, c, and d might be caused by both nonuniform p_0 profiles, changes in shock shape, and in turn the local flow-field effects on heat-transfer rate on the wind surfaces.

Prior to the Viking entry, several runs were made on a 14-in.-diam hemisphere-cylinder at conditions essentially the same as those of the Viking test. These tests were conducted to establish the effects of particle disturbances, flow contamination, and flow profiles on a large blunt body having a well-defined pressure and heat-transfer-rate

distribution. Data from the hemisphere-cylinder test are shown in Fig. A-6, and comparisons are made with analytical heat-transfer and pressure data. The agreement is quite reasonable. Note that there is no apparent effect of shock oscillations or nonuniform pitot pressure distribution on the hemisphere data. Therefore, it cannot be concluded that deviations in shock shape alone produce the large scatter in the windward surface heat-transfer data.

Nonuniform Flow Field Effects

Calculations have also been performed using the Barnwell blunt-body program (Ref. 11) for the 70-deg cone Viking aeroshell geometry. These calculations were not intended to provide quantitative assessments of the effect of a free-stream nonuniform pitot pressure distribution but rather to indicate the order of sensitivity of the front-face body pressure distribution to free-stream nonuniformities. It was found that a distribution of 0.1 percent in free-stream velocity from the model stagnation point to the outer radius produced a 12-percent change in local pressure near the extreme radius. The uncertainty in free-stream parameters is considerably greater than the 0.1-percent velocity perturbation necessary to significantly disturb the body data. One is led to conclude that very blunt bodies having sonic corners are extremely sensitive to small amounts of free-stream nonuniformities and that blunt models should be as small as possible to minimize these effects.

Note: Windward and leeward data channels are on approximately same sensitivities.

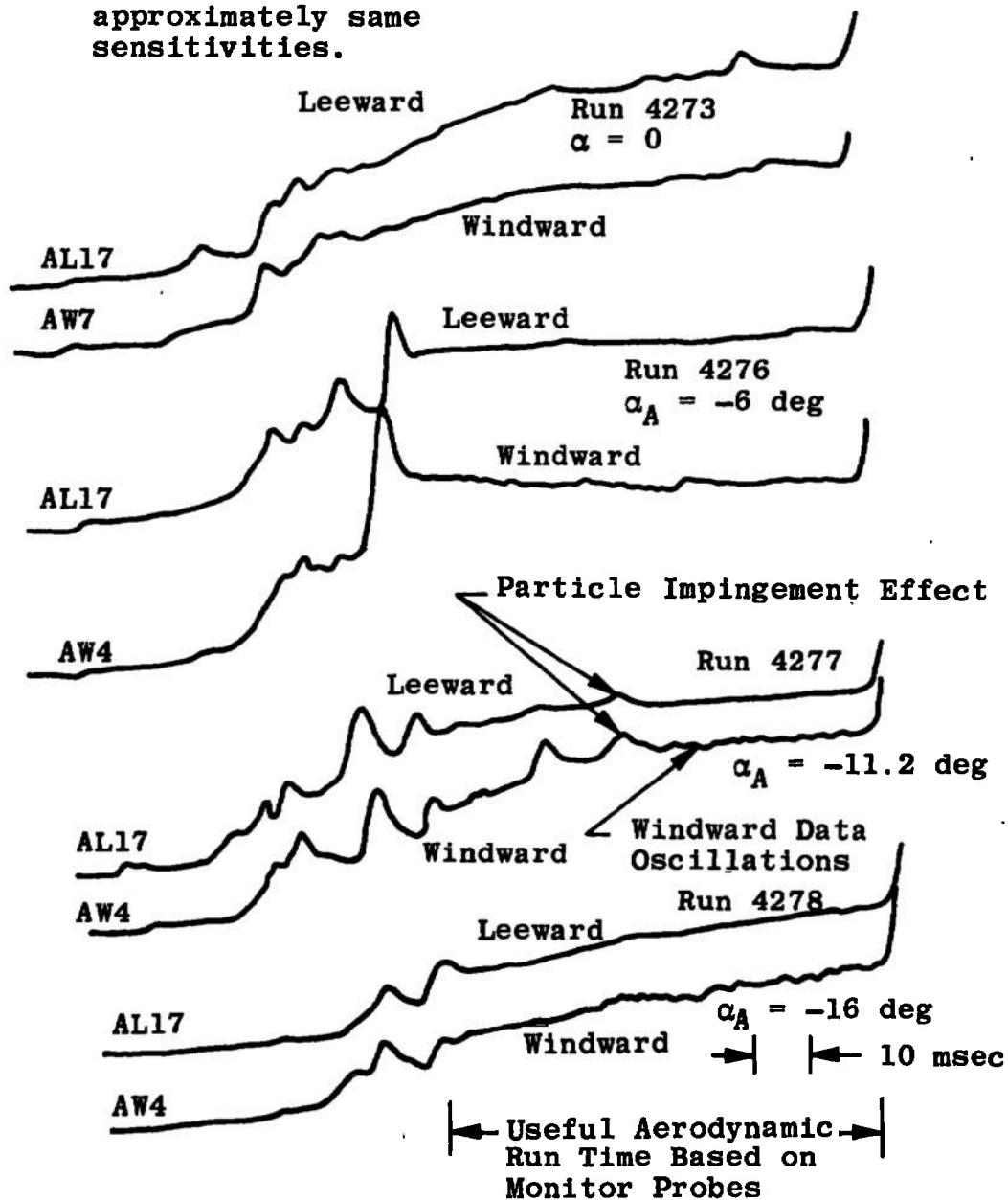


Figure A-1. Comparisons of aeroshell (front face) windward and leeward heat-transfer-rate analog signals.

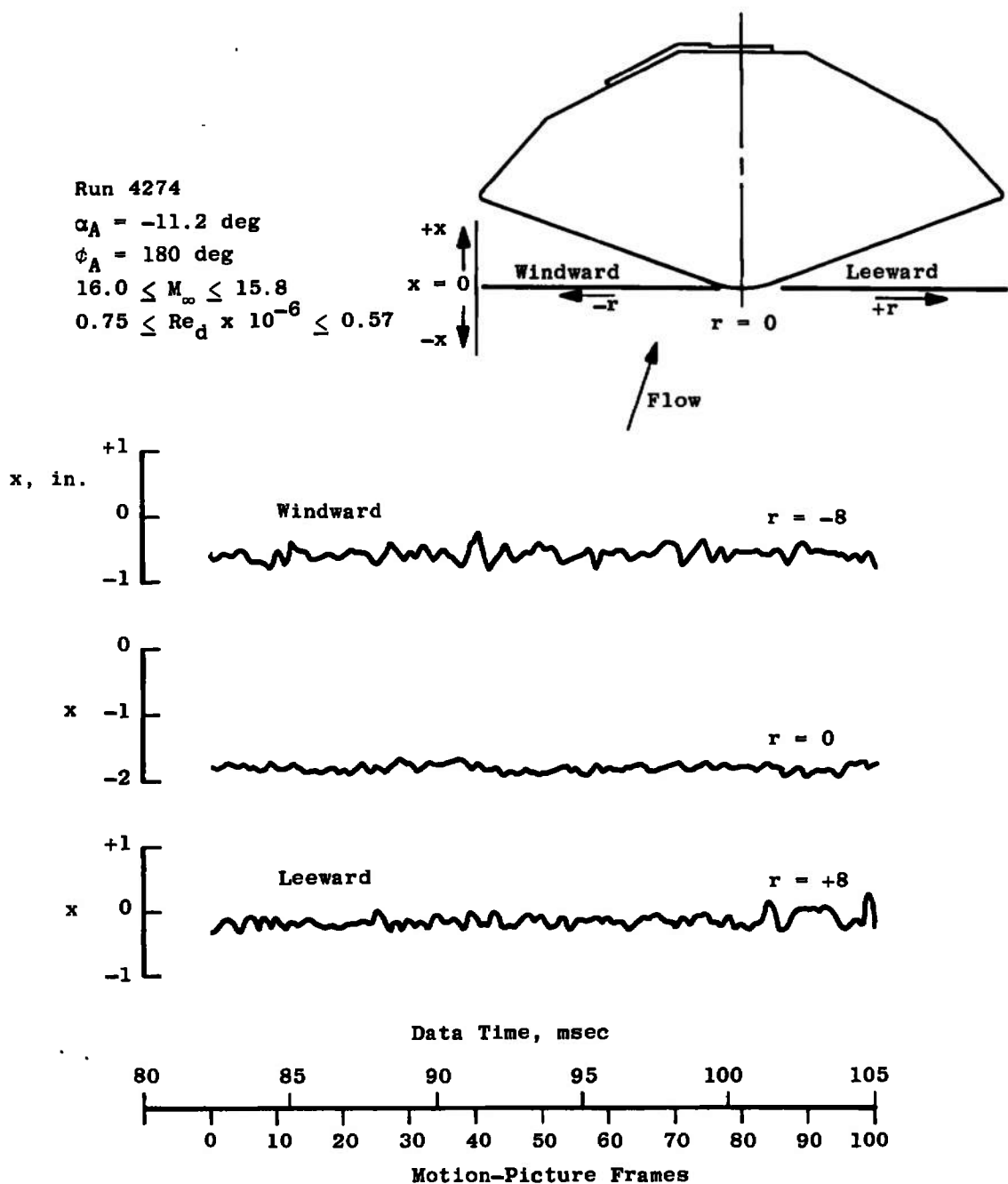


Figure A-2. Front-face bow shock oscillations.

Sym	Run	ϕ_A , deg	t, msec	M_∞	$Re_d \times 10^{-6}$
▲	4273	180	100	15.2	0.59
■	4274	↓	90	15.7	0.71
●	4279	↓	100	15.9	0.59
◆	4282	↓	100	15.8	0.65
◐	4283	↓	100	16.5	0.77
△	4266	0	100	15.7	0.56
□	4268	↓	100	15.9	0.74
○	4269	↓	100	15.5	0.58
◇	4270	↓	100	15.7	0.53
◊	4271	↓	100	16.2	0.91

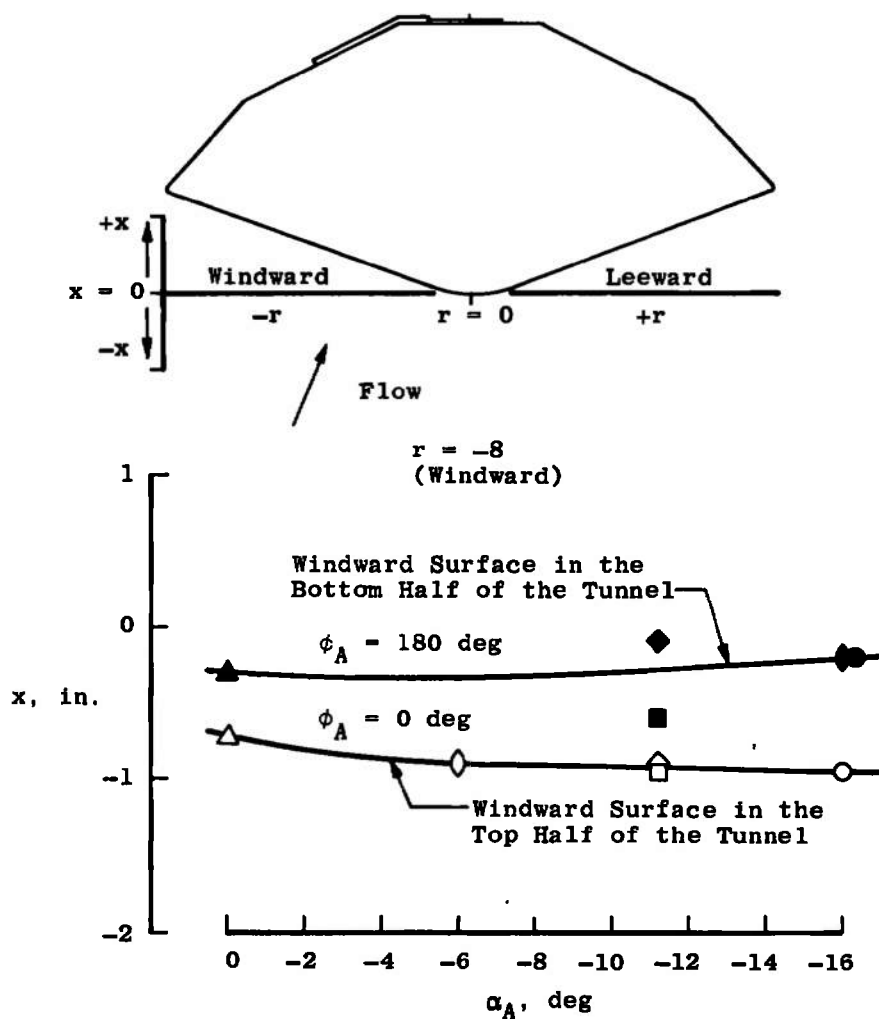


Figure A-3. Variation of bow shock location with angle of attack, $r = -8$ in.

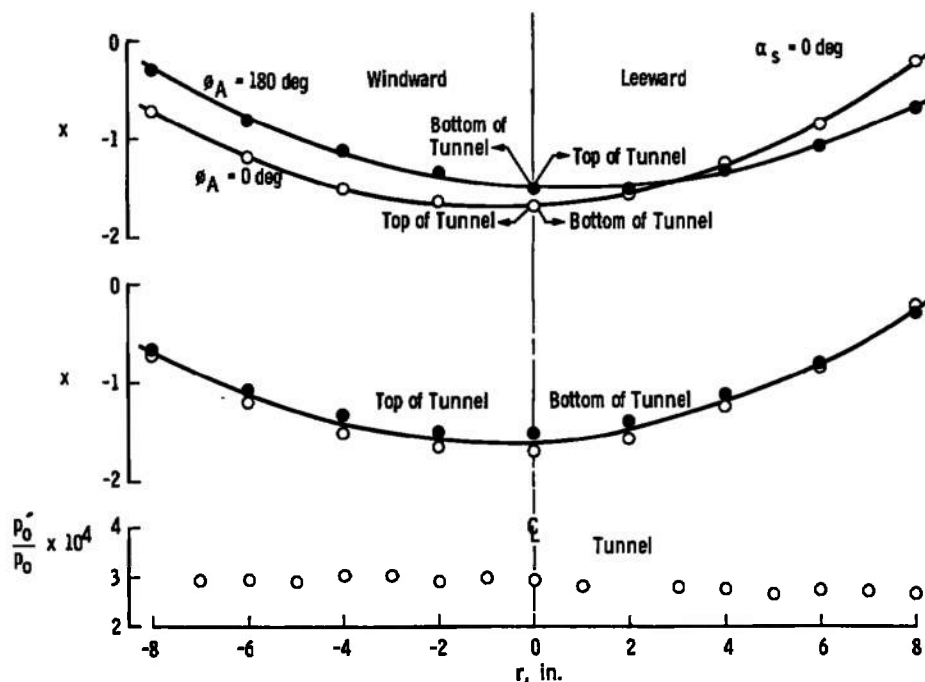


Figure A-4. Bow shock shapes at zero angle of attack.

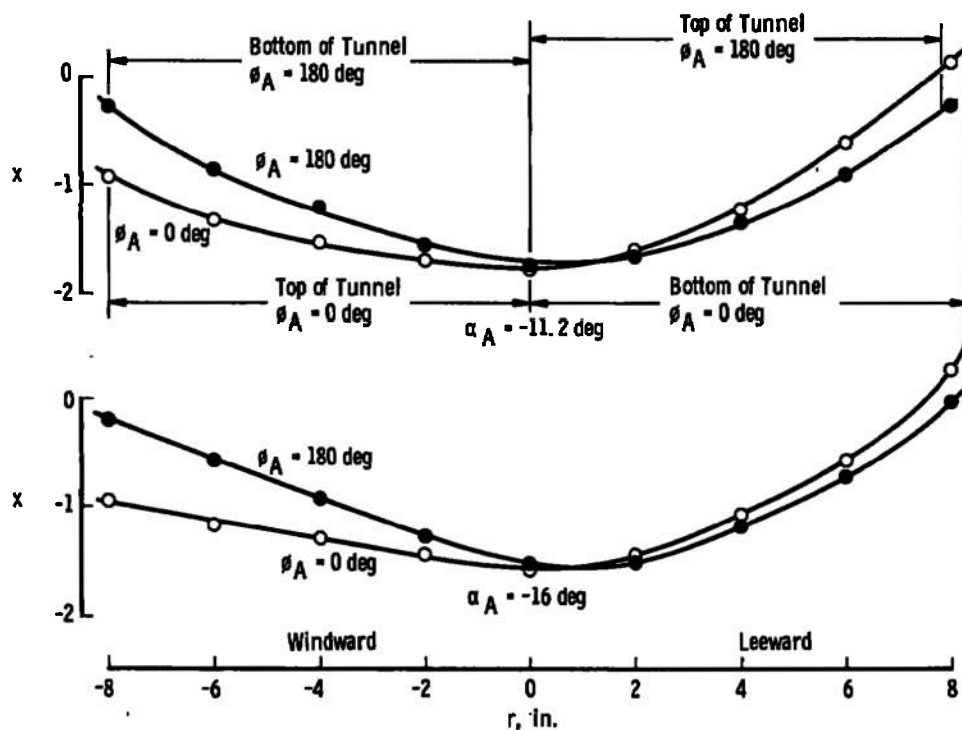


Figure A-5. Bow shock shapes at $\alpha_A = -11.2$ and -16 deg (model orientation).

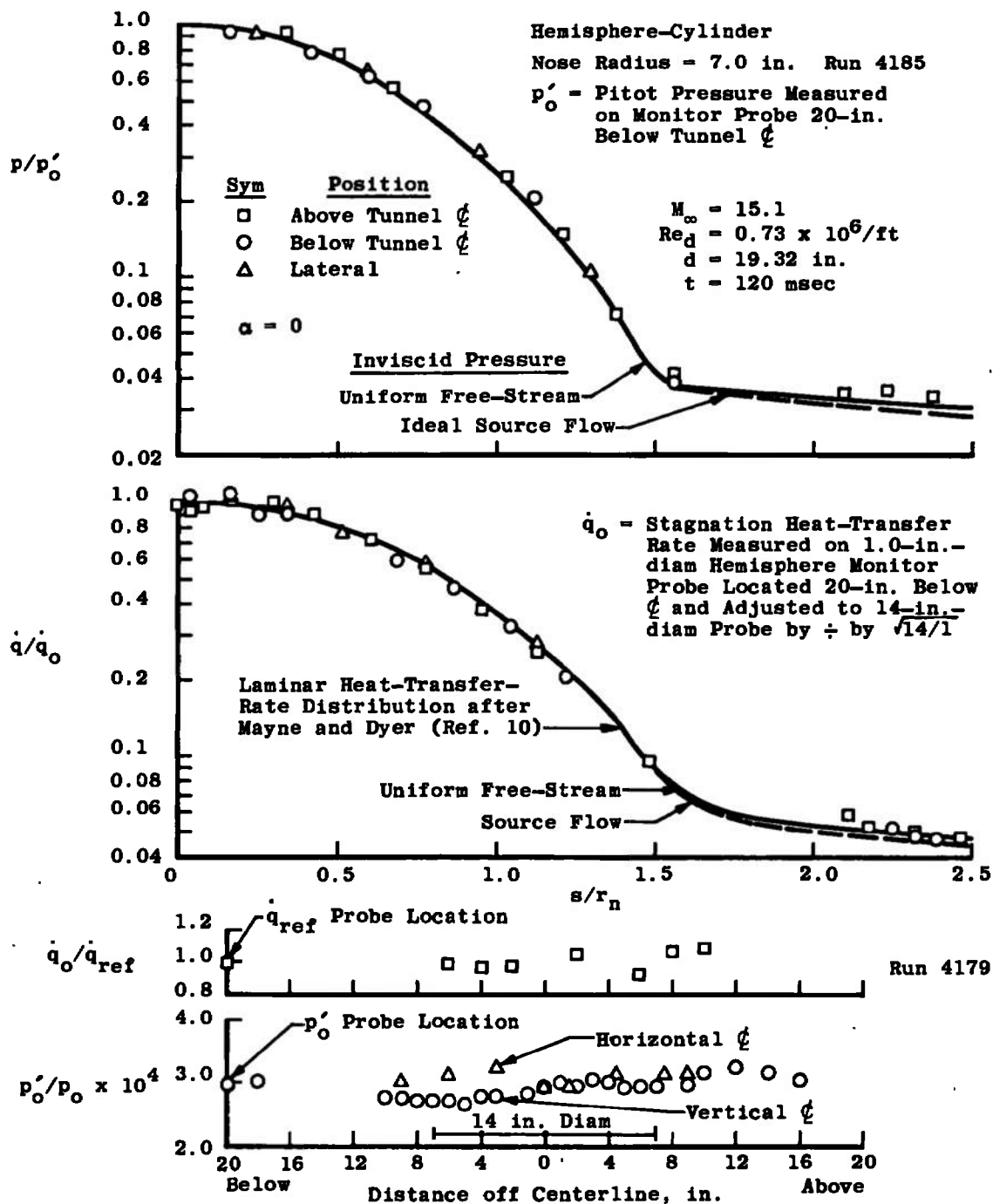


Figure A-6. Pressure and heat-transfer-rate distributions on a 14-in.-diam hemisphere-cylinder model in Tunnel F at Mach number 16.

NOMENCLATURE

d	Diameter of Viking model, 19.32 in.
H_o	Stagnation enthalpy, Btu/lb _m
M_∞	Free-stream Mach number
p	Pressure, psia
p_b	Base pressure measured on model sting, psia
p_o	Measured arc chamber pressure, psia
p_o'	Measured stagnation pressure behind free-stream normal shock, psia
p_∞	Free-stream pressure, psia
\dot{q}	Measured heat-transfer rate, Btu/ft ² -sec
\dot{q}_L	Local heat-transfer rate determined from undisturbed aeroshell windward ray heating distribution (see Section 4.0), Btu/ft ² -sec
\dot{q}_o	Stagnation point heat-transfer rate to a 4.83-in. radius hemisphere inferred from shoulder measurements on 0.5- and 1.0-in.-radius hemisphere cylinders, Btu/ft ² -sec
q_∞	Free-stream dynamic pressure, psia
Re_d	Reynolds number based on diameter of Viking model
r	Distance from model centerline measured normal to centerline, in.
r_b	Base radius of Viking model, 9.66 in.
r_n	Nose radius of Viking model, 4.83 in.
r_p	Radius of heat-transfer monitor hemisphere-cylinders, in.
St_o	Stanton number of reference heat-transfer rate \dot{q}_o . $St_o = \dot{q}_o / \rho_\infty U_\infty (H_o - H_w)$
s	Surface distance on model from zero-incidence stagnation point
T_o	Stagnation temperature, °R
T_w	Model wall temperature, ~540°R

T_{∞}	Free-stream temperature, °R
t	Time initiated at start of tunnel run, msec
U_{∞}	Free-stream velocity, ft/sec
x	Axial distance of bow shock from model nose (see Fig. A-2)
α_A	Effective angle of attack of model aeroshell, deg
α_{BC}	Effective angle of attack model base cover, deg
α_S	Pitch angle of model body centerline, deg
θ	Angle of tangent to point on model face with respect to model centerline, deg
θ_C	Viking model front-face cone half-angle, 70 deg
ρ_{∞}	Free-stream density, lbm/ft ³
ϕ	Angular position on model surface with respect to aeroshell windward streamline, deg
ϕ_A	Rotational position of aeroshell with respect to model body, deg